Title
THE PRODUCTION OF PHOTOMESONS FROM HELIUM

Author
Jakobson, Mark J.

Publication Date
1951-05-25

Copy 2

UCRL-1317

UNCLASSIFIED

UNIVERSITY OF CALIFORNIA — BERKELEY

RADIATION LABORATORY

DISCLAIMER

UCRL-1317
Unclassified - Physics Distribution

UNIVERSITY OF CALIFORNIA

Radiation Laboratory

Contract No. W-7405-eng-48

THE PRODUCTION OF PHOTOMESONS FROM HELIUM

Mark J. Jakobson

(Thesis)

May 25, 1951

Berkeley, California

The Production of Photomesons from Helium

Table of Contents

I. ABSTRACT

A study has been made of the mesons produced from helium by bombarding a high pressure target with the 312 ±15 Mev bremsstrahlung beam of the Berkeley Synchrotron. Measurements were made at the three angles of 45°, 90°, and 135° to the beam direction. Scintillation counter detectors, using $\pi^+ - \mu^+$, $\pi^+ - \beta^+$, and $\pi^+ - \mu^+ - \beta^+$ delayed coincidence techniques, were used at 90° and 135°. Ilford C-2 emulsions were used as detectors at 45°. The minimum energy detected was about 35 Mev, due principally to the energy loss of the mesons in the target walls. Bombardments were also carried out on hydrogen giving hydrogen-helium ratios.

The energy spectra of π^+ mesons from hydrogen and helium have been obtained for the three angles, as well as the π^- energy spectrum for helium at 45°. The ratio of π^- to π^+ mesons from helium at 45° is 0.99 ± 0.15. Differential and total cross sections for π^+ production were evaluated extrapolating from the minimum energy detected to zero meson energy. The results are presented in the following table (not corrected for nuclear absorption).

Gas	$\frac{d\sigma(\theta)}{d\Omega}$ cm^2 (steradian)$^{-1}$(equivalent quantum)$^{-1}$(proton)$^{-1}$ Angle			σ cm^2(equivalent quantum)$^{-1}$(proton)$^{-1}$
	45° + 17° − 15°	90° ± 19°	135° + 19° − 21°	
Helium	$2.5 \pm .2 \times 10^{-30}$	$4.0 \pm .3 \times 10^{-30}$	$3.2 \pm .2 \times 10^{-30}$	$4.1 \pm .2 \times 10^{-29}$
Hydrogen	$5.5 \pm .5 \times 10^{-30}$	$7.4 \pm .5 \times 10^{-30}$	$5.4 \pm .4 \times 10^{-30}$	$7.8 \pm .4 \times 10^{-29}$
Ratio $\frac{\text{Helium}}{\text{Hydrogen}}$	.45 ± .06	.54 ± .05	.59 ± .06	.53 ± .04

In addition to the standard deviations indicated, a systematic error of $\pm$ 20 percent is present in the total cross sections due to uncertainty in beam integration.

II. INTRODUCTION

Previous to 1948 the experimental investigation of the properties of mesons was limited to cosmic ray studies. The detection, by Gardner and Lattes[1] in 1948, of mesons artificially produced by high energy nucleons, and in 1949 of mesons artificially produced by high energy photons (McMillan and Peterson[2]), made possible a more extensive investigation of the properties of mesons.

Early in 1949 McMillan, Peterson, and White[3] carried out an exploratory experiment, using plates, on the photoproduction of mesons from carbon. This was followed later with a more complete experiment by Peterson, Gilbert, and White[4] in which energy spectra at three angles, the total cross section, and a value for the π^-/π^+ ratio was obtained.

Photoproduction of mesons from hydrogen was first undertaken by Cook,[5] using a liquid hydrogen target and nuclear emulsion detectors. While in progress, an electrónic method of π^+ meson detection was developed by Steinberger and Bishop.[6] Using this method, they measured an excitation function, an angular distribution for one photon energy, and an energy distribution at 90° to the photon beam direction.[7,8] Both polyethylene-carbon subtraction and the liquid hydrogen target of Cook were used for these measurements. Mozley,[9] using the electronic method of detection developed by Steinberger and Bishop,[6] measured the production of π^+ mesons as a function of atomic number for meson energies of 42 Mev and 76 Mev at an angle of 90°.

More recently, values of π^-/π^+ ratios have been obtained for several light elements (Littauer and Walker[10]). The production of photomesons from deuterium has been investigated by White.[11]

Helium is of interest since it is the simplest tightly bound nucleus. Although it is too complicated to predict rigorous theoretical results, the ratio of π^- to π^+ mesons from helium, and the ratio of helium meson production to that of carbon and hydrogen, may serve to give an insight into nuclear structure.

III. DESCRIPTION OF THE EXPERIMENT

The study was made by bombarding a pressure target, containing helium, with the beam of photons from the Berkeley Synchrotron. The photons were produced in the synchrotron by 312 $\pm$ 15 Mev electrons spiraling into a 0.02 in. platinum target on the inner side of the accelerating tube. The spread-out photon beam was used for the experiment. The beam of photons emerged in a narrow cone of 0.0135 radians at half intensity. In order to reduce background in the detectors the photon beam was collimated by three lead collimators as illustrated in Fig. 1. The near edge of the 9 in. primary collimator was located 55 in. from the photon source. The hole in the collimator was tapered parallel to the diverging photon beam. The diameter of the smaller end of the hole was 3/4 in. The second and tertiary collimators were 1 in. and 1-1/2 in. in diameter respectively. The purpose of the secondary collimators was to shield the target walls from the spray of electrons, positrons, and photons produced in the walls of the primary collimator. The intensity of the photon beam was essentially unchanged in going through the gas in the target. The attenuation was less than 2 percent over the length of the target.

The target consisted of a stainless steel pressure cylinder surrounded by a liquid nitrogen jacket, which is in turn contained in a vacuum chamber. The center of the target was 39 in. from the primary collimator, making the diameter of the beam 1.45 in. at emergence from the target. The pressure cylinder of the target was 2 in. in diameter, sufficiently large so that the beam did not strike the target walls.

The beam was integrated using two integration chambers, one ahead

of the collimating system, and one behind the target.[12] Ratios of the readings were plotted for consistency and found to agree within 2 percent.

The π^+ mesons were detected using both counters and plates. Surrounding the target was an assembly to hold the crystals and plates. A photograph of the assembly is shown in Fig. 2 and a drawing of the components is shown in Fig. 3. The plates were used for the π^-/π^+ ratio since both positive and negative mesons could be detected. Due to the high accidental background at 45°, the counters were used to obtain data at only 90° and 135°. The holder for plates and crystals is comprised of five wing-like sections jutting out from the target. Each section contains a 45°, 90°, and 135° channel defined by uranium edges. The remainder of the channel is made of lead held in place by 1/2 in. dural.

The plates were surrounded on all sides by lead to give sufficiently "poor" geometry to compensate for multiple Coulomb scattering in the absorbers. The plates were placed such that the emulsions were along a radius drawn from the target center. Five plates were located at each target position, sandwiched between ten glass slides of the same stopping power. The center of each plate was about 9 in. from the target center. Each of the four plate holders had a different amount of lead absorber for the same angle. This permitted simultaneous exposure of 4 energies at each of the three angles with the plates. The bottom section, or holder, containing the crystals was constructed so that the absorbers could be varied.

The electronic detection made use of three delayed coincidence schemes. In the first method of detection,[13] photomultiplier pulses from a meson passing through one crystal and stopping in a second opened a gate 0.08 μ seconds long and delayed 0.025 μ seconds. If the μ^+ pulse from the decay of the stopped π^+ occurred during the time the gate was open, the

meson was counted by $\pi^+ - \mu^+$ coincidence. In the second method[6] the $\pi^+ - \mu^+$ decay was unresolved and a set of four consecutive 2 μ second gates delayed 0.4 μ seconds from the initial event was used for the delayed coincidences. If the β^+ pulse occurred during the time one of the gates was open, the meson was counted by a $\pi^+ - \beta^+$ coincidence.

By combining the two methods, mesons were counted by a $\pi^+ - \mu^+ - \beta^+$ coincidence. This required that a meson stop in a crystal, the μ^+ meson from the π^+ decay remain in the crystal, and the β^+ from the μ^+ decay have sufficient energy loss to be counted.

The plates were exposed and counter data obtained in one long run. Operating voltages for the counters were established at the beginning of the run. A polyethylene target was used for this purpose to give a higher counting rate. A well-defined plateau was not obtained for the pulses from mesons stopping in the crystal. For this reason, the efficiencies of the counters were determined by data from the plates.

With the empty target, no mesons were counted in an interval when seventy-five would have been expected from the target filled with helium. This was checked later by plate data. Five σ mesons were found from hydrogen in an area yielding 320 π^+ mesons. Since hydrogen is believed to yield no π^- mesons, the σ's are due to cosmic rays or production in the target assembly. The fact that the σ's were coming from the target direction indicated the latter. Since the effect was of the order of 2 percent or less, the background from the target was considered negligible. The minimum energy detected was about 35 Mev due to energy loss by the mesons in the target and in the target walls.

The plates were developed using standard procedure and scanned using microscopes of 250-500 power. Approximately 30 cm^2 were scanned for

helium and 23 cm^2 for hydrogen. The thickness of the emulsions before development was determined by exposing the plates to high energy alpha particles. The alpha particles were sent through the emulsions at an angle of 45° to the surface. Assuming shrinkage only in the thickness, the projected path length after development is equal to the original thickness of the emulsion.

The results were corrected for decay in flight, penetration of the collimating edges, multiple scattering, and nuclear absorption. The cross sections are expressed in terms of equivalent quanta.[4] No corrections were made for deviations from a true bremsstrahlung distribution due to scattering, absorption, and modulation of the rf for the spread out beam. Such corrections would not affect the relative values, only the total cross section. The maximum uncertainty in the total cross is $\pm$ 20 percent due to uncertainty in beam integration.[14]

IV. TARGET ASSEMBLY

A. Target Construction

The pressure target used was that of R. S. White, and is the same general type as that used by Panofsky et al.[15] In order to minimize background from the ends of the target, a long (24 in.) target was constructed. The target is illustrated diagrammatically in Fig. 3.

The high pressure chamber was an 80 mil stainless steel cylinder 2 in. in diameter, 24 in. long, capped by hemispherical shells of 42 mil thickness at each end. The chamber has a safety factor of at least 4 when operated at 2200 p.s.i. and liquid nitrogen temperature. Normal operating pressure was 2200 p.s.i. The safety factor is less at room temperature since stainless steel decreases in strength as the temperature rises. Five-sixteenths inch of liquid nitrogen contained in a 12 mil stainless steel jacket surrounds the sides of the cylinder. Two stainless steel pipes lead from the jacket to the bottom and top of a liquid nitrogen reservoir. This serves to keep bubbling in the jacket from blowing liquid nitrogen away by percolating it back into the reservoir.

The pressure chamber and nitrogen cooling system are enclosed in a vacuum to keep moisture and ice from collecting on the target.

B. High Pressure System

Fig. 4 is a schematic of the high pressure system. The pressure lines from external connections to the pressure chamber were cooled by passing them through the liquid nitrogen reservoir. One of the lines was connected to a 3500 p.s.i. safety blow off valve. Its purpose was to prevent the pressure from increasing to a danger point if the target was not cooled properly. The other line was connected through a stainless

steel liquid nitrogen trap to a tank of helium. The helium tank was filled to an initial pressure of 2200 p.s.i., eliminating the need for a high pressure pump. Since the hydrogen tanks are filled to only 1700 p.s.i., a pump was required to raise the pressure to operating pressure. The pressure was measured by a 3000 p.s.i. (maximum) gauge, 20 lbs/division, calibrated with an Ashcroft gauge tester. The calibration was accurate to ± 20 p.s.i.

Thermocouple junctions were used to indicate the level of the nitrogen in the reservoir. One of the junctions was 2 in. from the bottom and the other one at the bottom. These would indicate when the liquid nitrogen was low. The temperature of the target was measured by a third thermocouple junction attached to the target. A Speedomax recorder was used to keep a record of the thermocouple readings. The time required for the precooled target to come to equilibrium after the gas was let in was approximately 1/2 hour.

C. Collimation System for Plates and Counters

Since the meson density decreases approximately as the inverse square of the distance from the target, it was desired to be as close to the target as possible. This makes desirable, absorbers of high relative stopping power. In order to be near the target and have a well-defined channel system the collimators had to be of relatively high stopping power material as well.

The limiting factor in the experiment was expected to be background due to electrons and positrons. Absorbing material which would provide the maximum decrease in this background was desired.

The choice of absorbing material can be made from two points of view:

either use low Z material to reduce conversion of photons, or high Z material to convert the photons and absorb the resulting electrons. The latter point of view was adopted and lead was selected for absorbing material in preference to copper. "Poor" geometry was selected to compensate for the multiple scattering.[16,17] Details of the collimation construction are given in the thesis of R. S. White.[11]

Uranium was chosen to line the channels because its high relative stopping power provided better angular resolution. The angular resolution, for plates, of both the 45° and 90° channels is illustrated in Fig. 5. The dotted line is the calculated angular resolution assuming the collimating edges opaque. The dark lines show the calculated values combined with the r.m.s. projected angle due to multiple scattering. The histogram is a plot of the angular distribution measured from plates.

The angular resolution for the channel was calculated in the following manner: Let $f(\theta)$ be proportional to the number of mesons entering the detector at any angle. Then:

$$f(\theta) = \iint \frac{dL\,dt}{r^2}$$

This can be shown to be

$$f(\theta) = \iint \frac{dL\,d\theta}{a}$$

Where, as illustrated in Fig. 6:

L = length of detector

r = distance of detector element dL from target element dt

t = effective length of target

a = perpendicular distance from element dL of detector to center line of target

θ = angle between center line of target and r

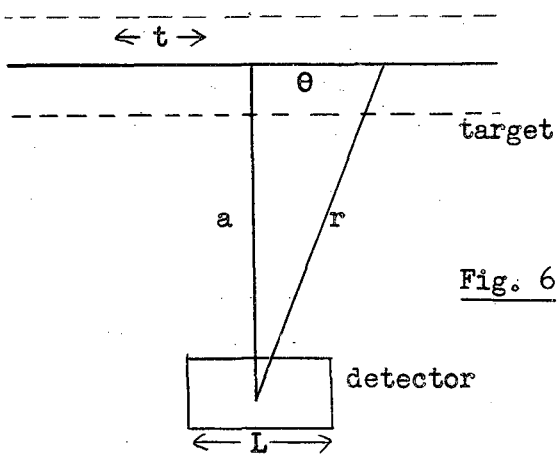

Fig. 6

This shows that for all angles where the entire width of the detector is unshielded by the collimators, $f(\theta) = \frac{L}{a}$. Hence the angular width at half height will be the difference between the two angles where $f(\theta) = \frac{L}{2a}$, or only 1/2 the detector is visible to the target.

To increase the angular resolution with the plates, a strip only 2 cm wide was scanned across the plates. The uncertainty in angle is larger with the counters, since the crystals are wider. The calculated angular widths at half height are given in Table I. The effect of multiple scattering can be neglected in this case since the angle subtended at the target by the r.m.s. displacement is approximately 3° for a meson energy of 80 Mev. This is the angle between the initial direction of the meson and a line drawn from the end of its path to its place of origin in the target.

TABLE I

Angular Resolution of Collimator

Detector	Angle	Angular Width
Plates	45°	$+ 17°$ $- 15°$
Plates	90°	$\pm 16°$
Counters	90°	$\pm 19°$
Counters	135°	$+ 19°$ $- 21°$

V. METHODS OF MESON DETECTION

A. Scintillation Counters

A block diagram illustrating the three delayed coincidence detection methods is presented in Fig. 7. The $\pi^+-\beta^+$ detection method used was that of Steinberger and Bishop.[6] Recent developments in electronics[18,19] and scintillation counters have reduced resolving times of amplifiers and coincidence circuits from $\sim 10^{-7}$ to $\sim 10^{-8}$ seconds, a time smaller than the half life of the π^+ meson, making possible π^+ decay detection electronically. Using these developments, a method of detection similar to that of Steinberger and Bishop[6] was developed using a delayed coincidence between a π^+ meson and its decay μ^+ meson.

Two trans-stilbene crystals with associated 1P21 photomultipliers were used as detectors. The photomultipler pulses, caused by a π^+ meson passing through one crystal and stopping in the second, opened a variable delay gate of width 0.08 μ second. The shortest gate delay used was 0.025 μ second, the longest delay was 0.19 μ second. If the μ^+ meson pulse arising from the decay of the stopped π^+ meson appeared during the time the gate was open, the meson was counted. A photograph of the $\pi^+-\mu^+$ coincidence circuit is shown in Fig. 8. The circuit diagram is illustrated in Fig. 9.

As a check that the particles identified by this method were mesons: (1) The maximum energy of the photon beam was reduced below threshold for π^+ production and no counts other than accidental background appeared. (2) The plateau obtained for the μ^+ pulse is quite flat, indicating uniform ionization loss, as would occur for a 4 Mev μ^+ meson arising from the decay of a stopped π^+ meson. (3) Combining the π^+ decay counting with the μ^+ meson decay scheme gives the expected number of $\pi^+-\mu^+-\beta^+$

coincidences.

As an application of this method, the π^+ meson mean life was measured by varying the gate delay.[20-23] Eight lengths of RG 63/U cable were used to provide the variable delay. The delay of each cable was measured, using a synchroscope, by photographing the reflections of pulses sent down the cable. Cable delays were measured to 2 percent. Fig. 10 is a plot of delay as a function of cable length. Fig. 11 is a plot of the π^+ decay curve. A value of $\tau_m = 2.54 \pm 0.11 \times 10^{-8}$ seconds was obtained for the mean life. This value agrees with references 23 and 24 but lies outside the standard deviations of previous measurements.

The accidental background for the $\pi^+ - \mu^+$ coincidence was obtained by delaying the gate for a time long compared to a π^+ mean life. This must be subtracted from the total number of counts obtained for a short delay to give the true number of meson counts.

For detection of mesons by $\pi^+ - \mu^+ - \beta^+$ coincidence, the output of the $\pi^+ - \mu^+$ detection was put in coincidence with the delayed coincidence from the first β gate. By delaying the μ^+ gate 19×10^{-8} seconds and putting the output of the $\pi^+ - \mu^+$ coincidence in coincidence with the output from the last β gate, the $\pi^\pm \mu^+ - \beta^+$ accidental background was obtained.

For the $\pi^+ - \beta^+$ detection, since the background was larger than the number of mesons, the accidental background for each β gate was given essentially by the last β gate. This value was in agreement with the value calculated by the usual accidental rate formula:

$$\frac{N_1 N_2 T}{d} = A$$

where T = width of gate + pulse width (sec)

N_1 = number of times the gate is opened $(\text{sec})^{-1}$

N_2 = number of pulses put in coincidence with the gate $(\text{sec})^{-1}$

d = duty cycle (fraction of time the beam is on)

A = accidental background $(\text{sec})^{-1}$

Since the duty cycle was unknown, it was calculated for a run by using the measured accidental rate. On the following run the duty cycle calculated from the previous run was used and a check obtained with the numerical value of the accidental background.

The background due to γ's from the uranium was negligible. The ratio of the background to the true meson count is presented in Table II for the three methods of counting.

TABLE II

Ratio of Background to True Meson Count

Detection Method	Average Background
$\pi^+ - \mu^+$	$\sim$ 0.1 - 0.2
$\pi^+ - \mu^+ - \rho^+$	$\sim$ 0.01
$\pi^+ - \rho^+$	$\sim$ 2. - 5.

B. Nuclear Emulsions

The emulsions used were Ilford C-2 emulsions since they are sufficiently sensitive for detection of $\pi^+ - \mu^+$ decays and yet minimize electron background. Electron tracks are not visible but appear as individual single grain background. Mesons are recognizable in C-2 emulsions by two characteristics, the rapid change in grain density and the large amount of small angle scatter in the last 100 microns of track.

Mesons coming to rest have three kinds of track endings. An event where the meson stops with no observable tracks leaving is called a ρ meson. An event where a meson comes to rest and a μ meson leaves the meson ending is a $\pi - \mu$ decay. The last type of meson, called σ, is one which comes to rest and one or more observable tracks, not identified as a μ

meson, leave the meson ending. It is apparent that a "one track" or "one prong" σ might be indistinguishable from a $\pi - \mu$ decay. According to Peterson, Gilbert, and White,[4] most one prong σ endings have "clubs" due to recoil nuclei. They assumed only 1 percent of all σ endings could be confused with a $\pi - \mu$ decay if the observer searched the endings for clubs.

More than 99 percent of all π^+ mesons ending in the emulsion decay into a μ^+ meson.[24,25] More than several thousand π^- endings have been observed without evidence that a $\pi^- - \mu^-$ decay occurs.[26] This therefore identifies the number of $\pi - \mu$ endings observed as the number of π^+ mesons observed.

The μ^+ mesons can only decay[27] and hence will appear as ρ mesons. Recent results indicate μ^- mesons produce stars a small fraction of the time.[28,29,30] The value quoted by George and Evans[30] is 0.055 ± 0.011. The remainder of the time the μ^- mesons either decay or are captured. Observations of π^- mesons stopping in C-2 emulsions indicate that 73 ± 2 percent form stars[31,32] with observable tracks, called σ mesons. The remainder appear as ρ mesons. Thus the number of π^- mesons coming to rest in the emulsion is: $\pi^- = 1.37\ \sigma$.

The number of ρ mesons observed is composed of 27 percent of the π^- mesons, the $\mu^\pm$ mesons due to decay of π's in flight, and the mesons from the $\pi - \mu$ decays.

The ratio of π^+ mesons to π^- mesons can be obtained by two methods. The first is:

$$\frac{\pi^-}{\pi^+} = \frac{1.37\ \sigma}{\pi - \mu}$$

The second method is based upon the following argument. The difference between the total number of mesons (T) of all types observed and the

number of π^- mesons observed is due to π^+ and μ^+ mesons. Assuming no $\mu^\pm$ production in the target, $\pi^+ = \mu^+$. Expressing this in terms of an equation: $T - 1.37\,\sigma = \pi^+ + \mu^+ = 2\,\pi^+$. The ratio obtained by this method is:

$$\frac{\pi^-}{\pi^+} = \frac{2}{\frac{0.73T}{\sigma} - 1}$$

The second expression was derived assuming no decay in flight. This is justified since the method is a difference method and decay in flight is a second order term.

The π^-/π^+ ratio as expressed by the first method depends only upon the emulsion, the observer, and the fraction of π^- mesons forming stars. The ratio as expressed by the second method depends, in addition, upon the assumption that ρ mesons are as easily identified as $\pi - \mu$ decays or σ's. For this reason the first method will be used to calculate ratios, the second merely to check the first.

VI. EXPERIMENTAL PROCEDURE

The alignment of the target at the synchrotron was done by means of a telescope and checked by exposing x-ray films. The high pressure fittings were tested by filling the target to 200 p.s.i. and brushing all connections with soapy solutions. During the bombardment liquid nitrogen was kept in the reservoir of the target 24 hours a day to insure equilibrium conditions.

To reduce accidental background the scalers were "gated" or operative only during the time the beam was on. The plates were exposed at the same time the counter data were being taken. Each energy spectrum was measured changing the absorber cyclically to avoid drifts in detection and integration that might distort the spectrum. Changing angles a number of times tended to cancel any drift distorting the relative values between angles. While getting ratios between gases, the gases were changed back and forth to again cancel drift. It required approximately 1/2 hour to change plates and gases.

In the coincidence counting schemes used it was advantageous to have as large a duty cycle as possible to reduce accidental background. At the synchrotron the duty cycle may be changed by modulating the rf so that the electrons spiral in more slowly, giving a beam spread out in time. A spread in energy also results since the electrons do not strike the target at a time corresponding to peak magnetic field. The spread, as estimated from the magnetic field curve[33] and time of emission, is $\sim$ 25 Mev. The beam length as measured on the synchroscope was of the order of 3300 μ seconds. The beam duration as calculated from the accidental rate was 2200 μ seconds, considerably shorter than that observed on the synchroscope. This is reasonable since the distribution of the beam in time is peaked and not flat.

The intensity level of the beam was limited by the accidental background of the counters for low meson energies where no absorber was used. Maximum beam could be used in almost all cases where absorbers were placed in front of the detectors. This permitted maximum exposures on the plates. The data sheet for a typical run is given in Table III.

TABLE III

Data Recorded for a Typical Run

	January 15, 1951			January 16, 1951				
Target	He			He				
Angle	135°			90°				
Absorber number	25			21				
Energy (Mev)	56			75				
Pressure (p.s.i.)	2210			2160				
Thermocouple #1	8.35			8.55				
Thermocouple #2	8.65			8.65				
Thermocouple #3	8.05			7.95				
Time of day	1805			1000				
ΔT run (minutes)	18	8.7	33	27.7	12.8	23.6	5.3	20.6
μ gate delay (10^{-8} seconds)	2.5	19	2.5	2.5	19	2.5	19	2.5
Back Integration chambers n Begin	90.56	94.79	97.08	180.63	185.76	188.04	192.26	193.50
Back Integration chambers n End	94.56	96.79	105.08	185.63	187.76	192.04	193.26	197.50
Front Integration chambers N Begin	346.98	386.00	379.0	792.80	818.30	829.04	850.0	856.36
Front Integration chambers N End	366.90	377.74	41849	817.20	827.80	849.10	855.08	876.10
Δ N/Δ n	5.02	4.87	4.94	4.85	4.75	5.01	5.08	4.93
(Scaler #1)μ gates x 64	66^{2}	98^{38}	232^{44}	86^{15}	118^{31}	192^{10}	209^{16}	284^{44}
$\Delta\mu$ gates x 64	66.0	32.5	134.0	86.2	32.2	73.8	17.1	75.3
(Scaler #2)$\pi-\mu$ coincidences x 64	0^{17}	0^{17}	0^{40}	0^{10}	0^{10}	0^{16}	0^{16}	0^{25}
$\Delta\pi-\mu$ coincidences	17	0	23	10	0	6	0	9

TABLE III (Cont.)

Data Recorded for a Typical Run

(Scaler #11) $\pi-\mu-\beta$ coincidences x 8	0^6	0^6	2^1	0^3	0^3	0^5	0^5	1^0
$\Delta\pi-\mu-\beta$ coincidences	6	0	11	3	0	2	0	3
(Scaler #4) Large Pulses Crystal #1 x 256	122.8	184.8	429.5	145.6	220.85	353.3	386.9	524.5
(Scaler #5) Large Pulses Crystal #2 x 256	95.3	143.3	338.5	119.1	165.1	262.7	287.2	389.4
(Scaler #6) β Gates x 256	14.3	21.7	51.1	17.9	24.9	39.8	43.5	58.7
(Scaler #3) Small Pulses Crystal #2 x 256	383	575	1347	418	580	917	1002	1352
(Scaler #7) $\pi-\beta_1$ Coincidences x 4	17^1	24^2	56^1	11^3	16^3	27^0	29^0	37^0
(Scaler #8) $\pi-\beta_2$ Coincidences x 4	15^3	23^1	53^3	11^2	13^2	20^3	22^0	29^0
(Scaler #9) $\pi-\beta_3$ Coincidences x 4	11^1	18^3	48^0	9^3	12^0	17^0	19^0	27^2
(Scaler #10) $\pi-\beta_4$ Coincidences x 4	10^1	14^3	42^0	7^0	10^2	16^3	18^3	26^0
Hi Voltage #1	1200			1200				
Hi Voltage #2	1150			1150				

VII. ANALYSIS OF DATA

A. Cross Section Calculations

Following the suggestion of McMillan, Blocker, and Kenney[34] and the precedent of Peterson, Gilbert, and White,[4] the cross sections will be expressed in terms of equivalent quanta. The number of equivalent quanta is defined as the total energy of the photon beam divided by the maximum energy of the photon beam. The total energy of the beam was obtained using the integration chamber calibrated by Blocker, Kenney, and Panofsky.[13]

By definition

$$\frac{d^2\sigma\,(E_\pi,\theta)}{dE_\pi\,d\Omega} = \frac{d^2N\,(E_\pi,\theta)}{dE_\pi\,d\Omega}\quad\frac{1}{n\,Q\,t}$$

where:

$\frac{d^2N\,(E_\pi,\theta)}{dE_\pi\,d\Omega}$ is the number of π mesons leaving the target per energy interval dE_π and solid angle $d\Omega$.

$\frac{d^2\sigma\,(E_\pi,\theta)}{dE_\pi\,d\Omega}$ is the cross section in cm^2 per proton for the formation of a π meson, per equivalent quantum, per energy interval dE_π and solid angle $d\Omega$

n is the number of protons per cm^3 in the target

Q is the number of equivalent quanta

t is the effective length of the target (cm)

Results are given per proton for the π^+ mesons and per neutron for the π^- mesons since the production of π^+ mesons is believed possible only from protons and π^- mesons only from neutrons.

For the purpose of calculation the differential cross section must be expressed in terms of measured parameters. Making the substitutions in the above expression:

$$\frac{d^2\sigma\,(E_\pi,\theta)}{dE_\pi\,d\Omega} = \frac{N}{\varepsilon}\quad\frac{1}{\int_t\int_L \frac{dt\,dL}{r^2}}\quad\frac{\Delta R}{\Delta E_\pi}\,\frac{1}{nQ}\,\frac{L}{W}$$

N = number of mesons/cm^2

$\mathcal{E}$ = efficiency of detection

L = length of detector (cm)

ΔR = depth of detector (cm)

ΔE_{π} = interval of meson energy at the target corresponding to the range interval ΔR of the detector (Mev)

W = thickness of the detector (cm)

t = effective target length (cm)

n = number of protons/cm^3

Q = number of equivalent quanta

r = distance of detector element dL from target element dt (cm)

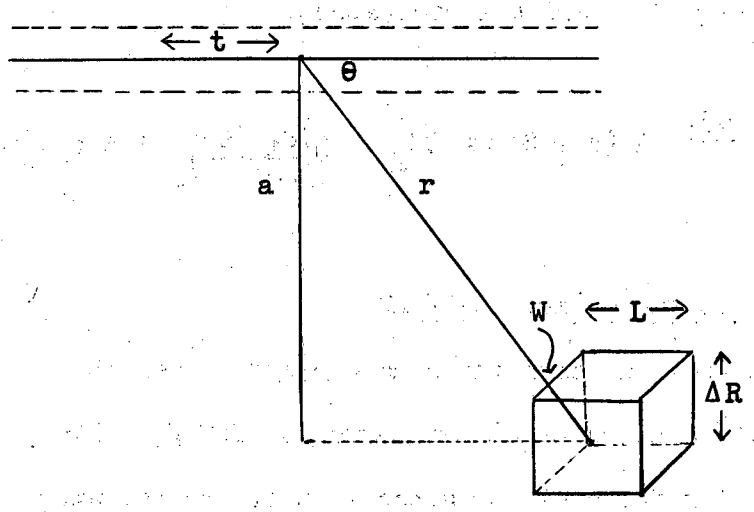

Fig. 12

The determination of the terms in the above expression for the cross section will be taken up in the following sections.

The differential cross section per unit solid angle is:

$$\frac{d\sigma_\pi\ (\theta)}{d\Omega} = \int_0^{E_{\pi max}} \frac{d^2\sigma\ (E_\pi,\ \theta)\ dE_\pi}{dE_\pi\ d\Omega}$$

This was integrated numerically by taking

$$\frac{d\sigma_\pi\ (\theta)}{d\Omega} = \sum_{i=0}^{E_{max}} \left(\frac{d^2\sigma\ (E_\pi,\ \theta)}{dE_\pi\, d\Omega}\right)_i \Delta E_{\pi i}$$

over the energy spectrum. For this evaluation it was necessary to extrapolate from the minimum energy detected to zero meson energy. The results are uncertain to the extent of the extrapolation. However, the ratios should be fairly independent of the extrapolation.

The total cross section is expressed:

$$\sigma_\pi = \int_\Omega \left(\frac{d\ \sigma_\pi\ (\theta)}{d\Omega}\right) d\Omega \quad \text{and was evaluated}$$

$$= 2\pi \int_0^\pi \left(\frac{d\sigma_\pi\ (\theta)}{d\Omega}\right)\ d\ (\cos\theta) \approx 2\pi \sum_{i=0}^{\pi} \left(\frac{d\sigma_\pi\ (\theta)}{d\Omega}\right)_i \sin\theta_i\ \Delta\theta_i$$

B. Determination of Meson Energy and $\Delta R/\Delta E$

The meson energy was determined using the range-energy curves of Aron, Hoffman, and Williams.[35] The range-energy curve for ICT #14 glass, calculated by Aron, was used for the emulsions since most of the "slowing down" occurs in the glass. In addition the curves for C-2 emulsions and ICT #14 glass are very nearly equal.

In order to get the meson energy for the counters, a range-energy

curve was calculated for trans-stilbene from curves for carbon and hydrogen, neglecting any effect of molecular binding. The resulting range-energy curves of mesons in trans-stilbene is given in Fig. 13.

$\Delta R/\Delta E$ was evaluated by the following method. A meson stopping at the back of the crystal would have a certain energy at entrance to the crystal. This was obtained from the thickness of the crystal and the range-energy relation in stilbene. The energy of entrance into the crystal is converted to an equivalent range in lead, the range of the absorber added, and the energy at entrance to the lead is obtained from the range-energy curve of lead. This procedure is carried out at each change of material until the center of the target is reached. By this method the energy of a meson leaving the center of the target and stopping at the back of the crystal is obtained. A similar calculation is done for a meson stopping at the front edge of the crystal. The range of the crystal divided by the difference of the two energies gives $\Delta R/\Delta E$ for the particular energy meson chosen. Repeating the procedure for a different thickness of absorber, a plot is obtained for $\Delta R/\Delta E$ as f(E).

C. Determination of the Number of Protons per Cubic Centimeter

Although helium is usually considered a better approximation to a perfect gas than hydrogen, at liquid nitrogen temperatures and 2200 p.s.i. helium[36] deviates farther from the perfect gas law than hydrogen,[37] making its density less than would be expected from the perfect gas law. No values of density measurements have been published in the region of liquid nitrogen temperatures and 2200 p.s.i. However, quite accurate extrapolation can be done using an equation of state. The density was calculated from the Beattie-Bridgeman equation of state, using constants evaluated

by S. W. Akin.[36] The resulting curve is shown in Fig. 14. The error in the number of protons/cm^3 as calculated by this method is estimated to be less than 3 percent.[38]

D. Determination of the Geometrical Factor

By geometrical factor is meant $\int_t \int_L \frac{dt\ dL}{r^2}$

from Section IV-C

$$\int_t \int_L \frac{dt\ dL}{r^2} = \int_L \int_{\theta_{min}}^{\theta_{max}} \frac{dL\ d\theta}{a}$$

where a = perpendicular distance from the center line of the target to the detector element dL

θ_{min} is the minimum angle from which mesons can reach any portion of the detector

θ_{max} is the maximum angle from which mesons can reach any portion of the detector

This integral was divided into three angular regions: one central region between θ_1 and θ_2 where all the length of the detector is visible to points of the target, and two regions where one collimating edge or the other obscures part of the detector. The contribution of the central region is equal to $\frac{L}{a}(\theta_1 - \theta_2)$ where the angles are in radians. The contribution of the other two regions was determined numerically by dividing the angle into increments $\Delta\theta$ and summing:

$$\int_0^L \int_{\theta_{min}}^{\theta_1} \frac{dL\ d\theta}{a} = \sum_{i\ \theta_{min}}^{\theta_1} \left(\frac{\Delta L}{a}\right)_i \Delta\theta_i$$ and similarly for

the other region. The resultant geometrical factors are given in Table IV.

TABLE IV

Geometrical Factors

Detector	Angle	Geometrical Factor	
Plates	45°, 135°	0.0608	(L = 2 cm)
Plates	90°	0.0460	(L = 2 cm)
Counters	45°, 135°	1.283	(L = 4.18 cm)
Counters	90°	0.920	(L = 4.18 cm)

E. Determination of Efficiency

The efficiency of the plates as a means of detection was taken to be 100 percent. The loss of mesons due to the failure to observe them near the surfaces of the emulsion was evaluated by plotting the number of mesons as a function of depth. This histogram is shown in Fig. 15. From the histogram it was estimated that the efficiency was constant up to within 2-1/2 microns from the surfaces and then decreased. As a result the data from the layers 2-1/2 microns thick at the surfaces was not used in calculating the results. This may not compensate for failure to observe mesons of short track length. Fig. 16 is a plot of the number of mesons as a function of track length. The calculated distribution is superimposed. The histogram indicates as much as 7 percent may be lost due to missing mesons of short track length, if it is assumed the calculated distribution is correct. Hence the efficiency for meson detection by plates is probably better than 90 percent. Rather than change the data by an unknown efficiency factor, the efficiency was taken to be 100 percent.

The absolute efficiency for the counters was determined from the plates. Plates exposed at 90° to the beam direction were scanned for 70 Mev mesons from hydrogen and deuterium.[11] The resulting points were used to adjust

the relative height of the counter curves. The ratio of hydrogen to deuterium points measured using plates and the ratio measured using counters are in excellent agreement. Using counter data alone, an expression for the number of mesons opening delayed gates can be obtained for the detection schemes assuming (1) no $\mu^{\pm}$ production in the target, (2) the efficiency of the $\pi-\mu-\beta$ detection is the product of the efficiencies of the $\pi-\mu$ detection and the $\pi-\beta$ detection. The expression resulting is:

$$N = \frac{N_{\pi-\mu} \quad N_{\pi-\beta}}{N_{\pi-\mu-\beta}}$$

where: N = number of mesons opening delayed gates

$N_{\pi-\mu}$ = number of mesons detected by $\pi-\mu$ coincidence

$N_{\pi-\beta}$ = number of mesons detected by the first β gate of the $\pi-\beta$ coincidence

$N_{\pi-\mu\beta}$ = number of mesons detected by the $\pi-\mu-\beta$ coincidence

The expression for the number of mesons opening delayed gates is independent of the efficiencies of the detection methods. The relative efficiencies as calculated from this equation are in agreement with those obtained from plate data. The efficiencies for the three detection methods as obtained from the plates is given in Table V.

TABLE V

Efficiency of Detection Methods

Detection Method	Efficiency Obtained from Plate Data
$\pi-\mu$	.076
$\pi-\mu-\beta$	.026
$\pi-\beta$	.256

F. Determination of the Number of Mesons/Cm^2

For the plates, the number/cm^2 is measured directly. For the counters, the number of mesons/cm^2 was obtained by dividing the number of mesons by the effective area of the stopping crystal. The effective area is less than the geometrical area $\Delta R \cdot L$. ΔR and L were defined in Section VIII-A. The difference is the area of a strip of length L and depth equal to the range necessary to produce the minimum ionization loss detected. The minimum energy loss required for a π^+ in the stopping crystal was 6 Mev. This corresponds to an effective area equal to 0.88 of the geometrical area.

G. Determination of Plate Thickness Before Development

The thickness after development was obtained by measuring the thickness at several points on each plate. Due to shrinkage in the development the thickness after development is less than the original thickness. The shrinkage factor was measured by exposing the plates to a small flux of high energy α particles. The plates were inclined 45° to the direction of the α particle beam. Assuming the shrinkage to be only in thickness (the emulsion keeps the same area), a measurement of the projected range after development is equal to the thickness before development. The value of the shrinkage factor obtained by this method was $2.42 \pm .12$.

H. Corrections Applied to Results

1. Multiple Scattering

The loss of mesons due to multiple scattering was calculated by the method of L. Eyges[17] and L. L. Foldy.[18] For plates, calculations showed the geometry was sufficiently "poor" that the correction was negligible. As many mesons scattered into the emulsion as out of the emulsion. The increase in path length due to the scatter could also be neglected.

For crystals, the loss due to multiple scattering is no longer negligible. The condition of "poor" geometry was valid in only one plane. This is because the width of the crystals was of the order of the width of the absorbers. Also the center of the stopping crystal was separated from the absorber by 4.4 cm.

The loss of mesons was obtained by the following method. The r.m.s. projected displacement as a function of meson energy (E) was calculated for a meson degraded from E_o at the target to E = 0 at the center of the crystal. (See Appendix A.) The r.m.s. displacement due to the stilbene was combined with the r.m.s. displacement due to the absorber. The resulting distribution is Guassian:

$$P(y) = \frac{1}{2\sqrt{\pi \langle \delta_E^2 \rangle}} \; e^{-\frac{y^2}{2\langle \delta_E^2 \rangle}}$$

where: y = coordinate perpendicular to the radius vector from the target, and the target center line

$\langle \delta_E^2 \rangle$ = r.m.s. projected displacement for energy E .

Since the loss at the center of the crystal is equal to the portion of the distribution function extending beyond the dimension of the absorber, for a given energy the fraction of mesons lost at the center of the crystal is equal to $1 - \mathrm{erf}\left(\frac{\sqrt{2}\ W}{4\sqrt{\langle \delta_E^2 \rangle}}\right)$ where W = width of absorber. Generalising to any point in the crystal:

$$\text{Fraction lost} = 1 - \frac{1}{2}\left[\mathrm{erf}\left(\frac{W-2x}{2\sqrt{2}\sqrt{\langle \delta_E^2 \rangle}}\right) + \mathrm{erf}\left(\frac{W+2x}{2\sqrt{2}\sqrt{\langle \delta_E^2 \rangle}}\right)\right] \text{ where:}$$

x = the perpendicular distance from a plane defined by the center line of the target and a radius vector to the center of the crystal.

The fraction lost was computed for 7 points in the crystal. A plot was made of the fraction lost as a function of distance from the center of the crystal, numerically integrated, and the average loss for the crystal as a whole obtained. The above process was repeated for 4 energies. The resultant correction curve as a function of energy is illustrated in Fig. 17. The corrections vary from 7 percent at 40 Mev to 27 percent at 140 Mev.

2. Decay in Flight

The loss of $\pi^{\pm}$ mesons due to decay in flight has been calculated assuming the mean life of the π^- meson[39,40] equal to the mean life of the π^+ meson.[12,21,22,23,24]

For N mesons detected, the number leaving the target would be $Ne^{t/\tau}$.

t = time of flight in meson frame

τ = mean life of π meson = 2.54×10^{-8} sec.

From the expression for time dilation and the relativistic equation for total energy of a π meson, the time of transit in the meson frame, between points a and b in the laboratory, is:

$$t = \frac{E_o}{c} \int_a^b \frac{dx}{\sqrt{T(T + 2E_o)}}$$

t = time (sec)

E_o = rest energy of π meson

T = kinetic energy of π meson

This equation was numerically integrated for various meson energies. The resultant correction is a maximum of 5 percent at the lowest energies and decreases to 2 percent for the higher energies.

The $\pi-\mu$ and $\pi-\mu-\beta$ coincidence detection, as well as the plates, must be corrected for loss due to decay in flight. For hydrogen, essentially no correction is necessary for the $\pi-\beta$ detection since the μ^+ resulting from a π^+ decay in flight will be detected. A correction must

be made for helium with π-β detection, since the μ^- mesons arising from π^- decay in flight will be detected.[41] This correction was ~3 percent.

3. Nuclear Absorption

Correction for the loss of mesons by nuclear interaction in the target, lead absorber, and detectors was made using a total absorption cross section equal to nuclear area.[42,43,44] This is in agreement with the values measured for poor geometry by Steinberger et al.[45] Nuclear area was calculated from $\sigma_{nucleus} = \pi(1.37\ A^{1/3} \cdot 10^{-13})^2$.[46] The correction increases from 8 percent at 35 Mev to 85 percent at 150 Mev.

4. Penetration of Collimating Edge

The geometrical factor as calculated in Section VII-D neglected any penetration of the collimating uranium. A correction was calculated making the assumption that the measured energy distributions could be replaced by flat spectra of equivalent area. With an absorber of sufficient thickness to detect a meson of energy E leaving the target, the maximum penetration is:

$$\Delta R = R(E_{max}) - R(E)$$

where: $R(E)$ = range in uranium of a meson of energy E

$R(E_{max})$ = range in uranium of a meson of energy equal to maximum energy of flat spectra

The collimating edge was then considered transparent up to a meson path of ΔR in the uranium and opaque beyond that value. The geometrical factor was recalculated using this new geometry to find the increase due to penetration. The correction is largest at low energies. The correction is less than 8 percent at 90° and less than 12 percent at 45°.

VIII. RESULTS OF THE EXPERIMENT

A. π^-/π^+ Ratio at 45°

For hydrogen, at 45°, 220 π^+ mesons were observed as compared to 3 σ mesons in the same area. At 90°, in an area yielding 100 π^+ mesons, 2 σ mesons were found. This data can be used to show either the number of π^- mesons produced by photons on hydrogen is less than 2 percent of the π^+ production, or the background due to the target assembly is less than 2 percent.

In the total area scanned for helium, at an angle of 45° to the beam, 88 σ, 122 π-μ, and 181 ρ mesons were observed. Using $\pi^-/\pi^+ = \frac{1.37\,\sigma}{\pi\text{-}\mu}$, the ratio of π^- to π^+ is 0.99 ± 0.15.

Theoretical calculations have been made by Brueckner[47] for π^-/π^+ ratios for free protons and neutrons. If one makes the assumption that the effect of other nucleons in the nucleus can be neglected, and compares the results from helium with the calculated curves, the experimental ratio is found nearer the theoretical curve which assumes a predominance of magnetic moment interactions. Since the theoretical curve neglecting magnetic moment interactions changes more rapidly with increasing angle, measurements of the ratios at larger angles would give more conclusive results.

B. Energy Spectra for Mesons from Hydrogen and Helium

The spectra of π^+ mesons from hydrogen and helium were plotted superimposed to obtain a comparison of their magnitudes. Figs. 18 and 19 indicate the consistency of the three electronic detection methods at 90° and 135°. The curves for the combined data are superimposed on the points from the three methods. Figs. 20, 21, and 22 show the energy

spectra for hydrogen and helium at 45°, 90°, and 135° (angles in the laboratory system). Smooth curves were drawn through the experimental points and extrapolated to zero meson energy to obtain the number of mesons emitted at each angle. The spectra of helium covers a larger energy interval than that of hydrogen, as would be expected due to the internal energy of the nucleons in the nucleus. Smooth curves of the energy spectra of hydrogen were combined for the three angles and are shown in Fig. 23. The maximum meson energy detected at 90° and 135° is above that calculated by conservation of energy and momentum for the given angle. This is understandable since the poor angular resolution permits mesons from other angles to reach the detector. The three energy spectra at 45°, 90°, and 135° for helium are presented in Fig. 24. The energy spectra for π^- mesons at 45° is shown in Fig. 25.

C. Total Cross Section for Production of π^+ Mesons from Hydrogen and Helium

The cross sections per steradian are illustrated in Fig. 26. These values, together with the total cross sections, and ratio of hydrogen to helium cross sections are presented in Table VI. The standard deviations indicated include both statistics of counting and measurements of the parameters listed in Section VII-A. Systematics not included are: + 7 percent for loss of events in scanning the plates, ± 20 percent for uncertainty in beam integration, and the uncertainty due to the extrapolation to zero meson energy.

TABLE VI

Cross Sections for Hydrogen and Helium

Gas	$\frac{d\sigma}{d\Omega}$ cm^2(steradian)$^{-1}$(equivalent quantum)$^{-1}$(proton)$^{-1}$ Angle			σ cm^2(equivalent quantum)$^{-1}$(proton)$^{-1}$
	45° $^{+17^\circ}_{-15^\circ}$	$90^\circ \pm 19^\circ$	135° $^{+19^\circ}_{-21^\circ}$	
Helium	$2.5 \pm .2 \times 10^{-30}$	$4.0 \pm .3 \times 10^{-30}$	$3.2 \pm .2 \times 10^{-30}$	$4.1 \pm .2 \times 10^{-29}$
Helium*	$3.1 \pm .3 \times 10^{-30}$	$4.7 \pm .4 \times 10^{-30}$	$3.8 \pm .3 \times 10^{-30}$	$4.8 \pm .2 \times 10^{-29}$
Hydrogen	$5.5 \pm .5 \times 10^{-30}$	$7.4 \pm .5 \times 10^{-30}$	$5.4 \pm .4 \times 10^{-30}$	$7.8 \pm .4 \times 10^{-29}$
Hydrogen*	$7.1 \pm .7 \times 10^{-30}$	$9.1 \pm .6 \times 10^{-30}$	$6.0 \pm .4 \times 10^{-30}$	$9.5 \pm .6 \times 10^{-29}$
Ratio $\frac{\text{Hydrogen}}{\text{Helium}}$	.45 ± .06	.54 ± .05	.59 ± .06	.53 ± .04
Ratio $\frac{\text{Hydrogen}}{\text{Helium}}$ *	.44 ± .06	.52 ± .05	.63 ± .06	.51 ± .04

* corrected for nuclear absorption

The decrease in production per proton in helium is due to both the increased binding energy of the nucleons and the exclusion principle.

D. Comparison of Results with Carbon

Comparison of the energy spectra of hydrogen, helium, and carbon is shown in Figs. 27, 28, and 29. The ratios of the cross sections are given in Table VII:

TABLE VII

Ratios of Cross Sections for Hydrogen, Helium, and Carbon

Gas	$\frac{d\sigma}{d\Omega}$ $cm^2(steradian)^{-1}(equivalent\ quantum)^{-1}(proton)^{-1}$ Angle 45°	90°	135°	$\sigma\ cm^2\ (equivalent\ quantum)^{-1}(proton)^{-1}$
Ratio $\frac{He}{H}$	.45 ± .06	.54 ± .05	.59 ± .06	.53 ± .04
Ratio $\frac{He}{H}$ *	.44 ± .06	.52 ± .05	.63 ± .06	.51 ± .04
Ratio C/H	.32	.36	.36	.35
Ratio C/H*	.33	.38	.41	.38
Ratio C/He	.71	.66	.59	.69
Ratio C/He*	.77	.74	.64	.75

* corrected for nuclear absorption

Standard deviations are not assigned to the carbon ratios due to uncertainty in beam integration.

The ratios determined by Mozley[9] were compared with the values plotted in Fig. 28. The values agree within statistics, indicating the efficiency of the beam monitor has probably not changed over a period of time. This indicates the difference in cross sections is probably real. The plates for the carbon were exposed using the spike x-ray beam. The experiment with helium and hydrogen was done with the spread out beam, which has slightly lower energy than the spike beam. This effect, although small, would tend to make the difference between carbon and helium more pronounced.

IX. APPENDIX

A. Calculation of r.m.s. Projected Displacement Due to Multiple Scattering

For a meson being degraded from energy E_{π_o} to energy E_{π} in passing through a material of thickness t, the distribution function upon emergence is given by:[17]

$$f(t,y,\theta) = \frac{1}{4\pi B^{1/2}} e^{\frac{-\theta^2 A_2 - 2y\theta A_1 + y^2 A_o}{4B}} \quad **$$

where, following the notation of L. Eyges:[17]

θ = angle between original direction of travel and the direction of travel at thickness t

$B = A_o A_2 - A_1^2$

$$A_o(t) = \int_o^t \frac{d\eta}{W^2(\eta)}$$

$$A_1(t) = \int_o^t \frac{(t-\eta)}{W^2(\eta)}\, d\eta$$

$$A_2(t) = \int_o^t \frac{(t-\eta)^2}{W^2(\eta)}\, d\eta$$

$$W = \frac{2P\beta}{E}$$

P = momentum of meson

β = relativistic velocity of meson

E = energy of meson

Integration over θ to get the distribution as a function of t and y:

$$f(t,y) = \frac{1}{2(\pi A_2)^{1/2}} e^{-y^2/4A_2}$$

** Note: In reference 17 the equation $F(t,y,\theta) = \frac{1}{2\pi B^{\frac{1}{2}}} e^{-\frac{\theta^2 A_2 - 2y\theta A_1 + y^2 A_o}{4A_o B}}$ should read $F(t,y,\theta) = \frac{1}{4\pi B^{\frac{1}{2}}} e^{-\frac{\theta^2 A_2 - 2y\theta A_1 + y^2 A_o}{4B}}$

To obtain the distribution function after leaving the material and entering air, make the transformation:

$$t = t$$

$$\theta = \theta$$

$$y = Y - L\theta \qquad \text{where: } L = \text{distance in air measured along original direction of travel}$$

Integrating the resulting distribution over θ to obtain the Y dependence:

$$F(t,Y) = \frac{1}{2\left(\pi (A_2 + 2LA_1 + L^2A_0)\right)^{1/2}} \; e^{-Y^2/4(A_2 + 2LA_1 + L^2A_0)}$$

This new distribution function is seen to be a Gaussian of increased width. The r.m.s. displacement is: δ r.m.s. $= \sqrt{2(A_2 + 2LA_1 + L^2A_0)}$. The constants A_0, A_1, and A_2 were evaluated by the method of L. L. Foldy.[18]

X. ACKNOWLEDGMENTS

My sincere thanks go to Professor Owen Chamberlain for guidance helpful advice during the course of this work. I am grateful to Alvin G. Schulz and R. Stephen White for their assistance in all parts of the experiment. Thanks are due Evan Bailey for assistance in preparing the thesis, Dr. Barkas and co-workers for suggestions as well as use of the facilities of the Radiation Laboratory Film Program, and Dr. Clyde Wiegand for timesaving suggestions in constructing the electronics. I also wish to thank Professor E. M. McMillan for his support and the entire synchrotron crew under George McFarland for ever present help in carrying out the bombardments.

XI. REFERENCES

1. E. Gardner and C. M. G. Lattes, "Production of Mesons by the 184-inch Berkeley Cyclotron," Science 107, 270 (1948)

2. E. M. McMillan and J. M. Peterson, "Production of Mesons by X-rays," Science 109, 438 (1949)

3. E. M. McMillan, J. M. Peterson, and R. S. White, "Production of Mesons by X-rays," Science 110, 579 (1949)

4. Peterson, Gilbert, and White, "Photomesons from Carbon," Physical Review 81, 1003 (1951)

5. L. J. Cook, private communication

6. J. Steinberger and A. S. Bishop, "The Detection of Artificially Produced Photomesons with Counters," Physical Review 78, 493 (1950)

7. A. S. Bishop, "The Photoproduction of Mesons from Hydrogen," UCRL-874, Ph.D. Thesis, University of California (1950)

8. Bishop, Steinberger, and Cook, "Production of Positive Mesons by Photons on Hydrogen," Physical Review 80, 291 (1950)

9. R. F. Mozley, "Production of π^+ Mesons by X-rays as a Function of Atomic Number," Physical Review 80, 493 (1950)

10. R. M. Littauer and D. Walker, "Production of Photomesons from Deuterium and Other Light Elements," Bull. Am. Phys. Soc. 26 (3), 15 (1951)

11. R. S. White, "Photomesons from Deuterium," Ph.D. Thesis, University of California (1951)

12. Blocker, Kenney, and Panofsky, "Transition Curves of 330-Mev Bremsstrahlung," Phys. Rev. 79, 419 (1950)

13. Jakobson, Schulz, and Steinberger, "Detection of Positive π Mesons by π^+ Decay," Phys. Rev. 81, 894 (1951)

14. W. Blocker, private communication

15. Panofsky, Aamodt, and Hadley, "The Gamma Ray Spectrum Resulting from Capture of Negative π Mesons in Hydrogen and Deuterium," UCRL-814

16. L. Eyges, "Multiple Scattering with Energy Loss," Phys. Rev. 74, 1535 (1948)

17. L. L. Foldy, "Multiple Scattering with Energy Loss," Phys. Rev. 75, 311 (1949)

18. Ginzton, Hewlett, Jasberg, and Noe, "Distributed Amplification," Pro. I. R. E. 36, 956 (1948)

19. C. Wiegand, "Distributed Coincidence Circuit," Rev. Sci. Inst. 21 (12), 975 (1950)

20. E. A. Martinelli and W. K. H. Panofsky, "The Lifetime of the Positive π Meson," Phys. Rev. 77, 465 (1950)

21. Kraushaar, Thomas, and Henri, "Detection of the π-μ Decay with a Scintillation Crystal," Phys. Rev. 78, 486 (1950)

22. Chamberlain, Mozley, Steinberger, and Wiegand, "A Measurement of the Positive π-μ Decay Lifetime," Phys. Rev. 79, 394 (1950)

23. C. E. Wiegand, "Measurement of the Positive π Meson Lifetime," UCRL-952 (1950)

24. F. M. Smith, "On the Branching Ratio of the π^+ Meson," Phys. Rev. 81, 897 (1951)

25. H. L. Friedman and J. Rainwater, "Experimental Search for the Beta-Decay of the π^+ Meson," Phys. Rev. 81, 644 (1951)

26. University of California Radiation Laboratory Film Group, private communication

27. Leighton, Anderson, and Seriff, "The Energy Spectrum of the Decay Particles and the Mass and Spin of the Mesotron," Phys. Rev. 75, 1432 (1949)

28. W. Y. Chang, "A Cloud-Chamber Study of Meson Absorption by Thin Pb, Fe, and Al Foils," Rev. Mod. Phys. 21, 166 (1949)

29. S. B. Jones and R. S. White, "Relative Energy and Angle Distribution of Low Energy π^- Mesons from 390-Mev Alpha Particles on Carbon. μ^- Meson Endings," Phys. Rev. 82, 374 (1951)

30. E. P. George and J. Evans, "Disintegrations Produced by the Nuclear Capture of Slow Negative μ-Mesons," Pro. Phys. Soc. 64 (2), 193 (1951)

31. F. L. Adelman and S. B. Jones, "Stars in Photographic Emulsions Initiated by π^- Mesons," Science 111, 226 (1950)

32. F. L. Adelman, "Fast Protons from the Capture of π^- Mesons in Photographic Emulsions," UCRL-1005, Ph.D. Thesis, University of California (1950)

33. G. Gauer and C. Nunan, "X-ray Beam Pulse Shaper for the Berkeley Synchrotron," UCRL-714 (1950)

34. E. M. McMillan, W. Blocker, and R. W. Kenney, "The r-Unit at 320 and 160 Mev," Phys. Rev. 81, 455 (1951)

35. Aron, Hoffman, and Williams, "Range Energy Curves," UCRL-121 2nd Rev. (1949)

36. S. W. Akin, "The Thermodynamic Properties of Helium," Trans. ASME 72, 751 (1950)

37. Johnston, Bezman, Rubin, Swanson, Corak, and Rifkin, MDDC-850.

38. S. W. Akin "Thermodynamic Properties of Helium at High Pressures and Temperatures," General Electric Co. Report No. 55141. Index No. NP-124

39. J. R. Richardson, "The Lifetime of the Heavy Meson," Phys. Rev. 74 1720 (1948)

40. Lederman, Tinlot, and Booth, "On the Decay of the π^- Meson," Phys. Rev. 81, 281 (1951)

41. H. K. Ticho, "The Capture Probability of Negative Mesotrons," Phys. Rev. 74, 1337 (1948)

42. U. Camerini, P. H. Fowler, W. O. Lock, and H. Muirhead, "Nuclear Transmutations Produced by Cosmic Ray Particles of Great Energy," Phil. Mag. 41, 413 (1950)

43. H. Bradner and B. Rankin, "Large Angle Scattering of π^- Mesons," Phys. Rev. 80, 916 (1950)

44. Bernardini, Booth, Lederman, and Tinlot, "Nuclear Interaction of π^- Mesons," Phys. Rev. 80, 924 (1950)

45. Chedester, Isaacs, Sachs, and Steinberger, "Total Cross Sections of π^- Mesons on Protons and Several Other Nuclei," unpublished results.

46. Fernbach, Serber, and Taylor, "The Scattering of High Energy Neutrons by Nuclei," Phys. Rev. 75, 1352 (1949)

47. K. A. Brueckner, "The Production of Mesons by Photons," Phys. Rev. 79, 641 (1950)

XII. ILLUSTRATIONS

Fig. 1 Schematic arrangement of the apparatus with respect to the synchrotron.

Fig. 2 Photograph of the target and collimator assembly.

Fig. 3 Drawing of a longitudinal and cross sectional view of the target and collimator assembly.

Fig. 4 Schematic drawing of the high pressure system.

Fig. 5 Angular distributions of mesons observed at the angles of 45° and 90°. Angular resolution of the 90° and 45° channels indicated. The abscissa is the angle from the beam direction.

Fig. 6 Diagram giving symbols used in geometrical factor.

Fig. 7 Block diagram of the electronics.

Fig. 8 Photograph of the $\pi-\mu$ coincidence circuit.

Fig. 9 $\pi-\mu$ coincidence circuit diagram.

Fig. 10 Plot of delay in RG 63/U cable as a function of cable length.

Fig. 11 π^+ meson decay curve. The number of mesons at each gate delay plotted against the gate delay.

Fig. 12 Diagram giving symbols used in cross section equation.

Fig. 13 Range of mesons in trans-stilbene.

Fig. 14 Pressure-density curve for helium in the region of 142 atmospheres for a temperature of 77.4° K.

Fig. 15 Plot of the depth distributions for the three types of mesons as a function of distance from the nearest surface. Includes energy spectra of the three angles.

Fig. 16 Plot of the projected track length in the emulsion for the 4 types of mesons. Includes data from energy spectrum of three angles. Length measurements accurate to ± 10 percent.

Fig. 17 Correction factor for loss of mesons due to multiple scattering plotted as a function of energy.

Fig. 18 90° energy spectra of π^{+} mesons from hydrogen and helium for the three electronic detection methods. The smooth curve is taken from the combined data. Extrapolation to zero meson energy is for the purpose of integration.

Fig. 19 135° energy spectra of π^{+} mesons from hydrogen and helium for the three electronic detection methods. The smooth curve is taken from the combined data. Extrapolation to zero meson energy is for the purpose of integration.

Fig. 20 45° energy spectra of π^{+} mesons from hydrogen and helium. Data taken from plates. The dashed curve shows the spectra corrected for nuclear absorption.

Fig. 21 90° energy spectra of π^{+} mesons from hydrogen and helium. A plot of combined data from the three electronic methods of detection. Extrapolated to zero meson energy for the purpose of integration. The dashed curve shows the spectra corrected for nuclear absorption.

Fig. 22 135° energy spectra of π^{+} mesons from hydrogen and helium. A plot of the combined data from the three electronic methods of detection. Extrapolated to zero meson energy for the purpose of integration. The dashed curve shows the spectra corrected for nuclear absorption.

Fig. 23 Comparison of energy spectra of hydrogen for three angles. Dashed curve shows the spectra corrected for nuclear absorption.

Fig. 24 Comparison of energy spectra of helium for three angles. Dashed curve shows the spectra corrected for nuclear absorption.

Fig. 25 Energy spectrum of π^- mesons from helium at an angle of 45°. Data taken from plates. Extrapolated to zero meson energy for the purpose of integration. The dashed curve shows the spectrum corrected for nuclear absorption.

Fig. 26 Average π^+ meson cross sections per steradian for hydrogen and helium. The smooth curve is drawn for the purpose of integration. The dashed curves show cross sections corrected for nuclear absorption.

Fig. 27 Comparison of π^+ meson energy spectra of hydrogen, helium, and carbon at 45°. Carbon data are taken from reference 4. Extrapolated to zero meson energy for the purpose of integration. The dashed curves show the spectra corrected for nuclear absorption.

Fig. 28 Comparison of π^+ meson energy spectra of hydrogen, helium, and carbon at 90°. Carbon data are taken from reference 4. Extrapolated to zero meson energy for the purpose of integration. The dashed curves show the spectra corrected for nuclear absorption.

Fig. 29 Comparison of π^+ meson energy spectra of hydrogen, helium, and carbon at 135°. Carbon data are taken from reference 4. Extrapolated to zero meson energy for the purpose of integration. The dashed curves show the spectra corrected for nuclear absorption.

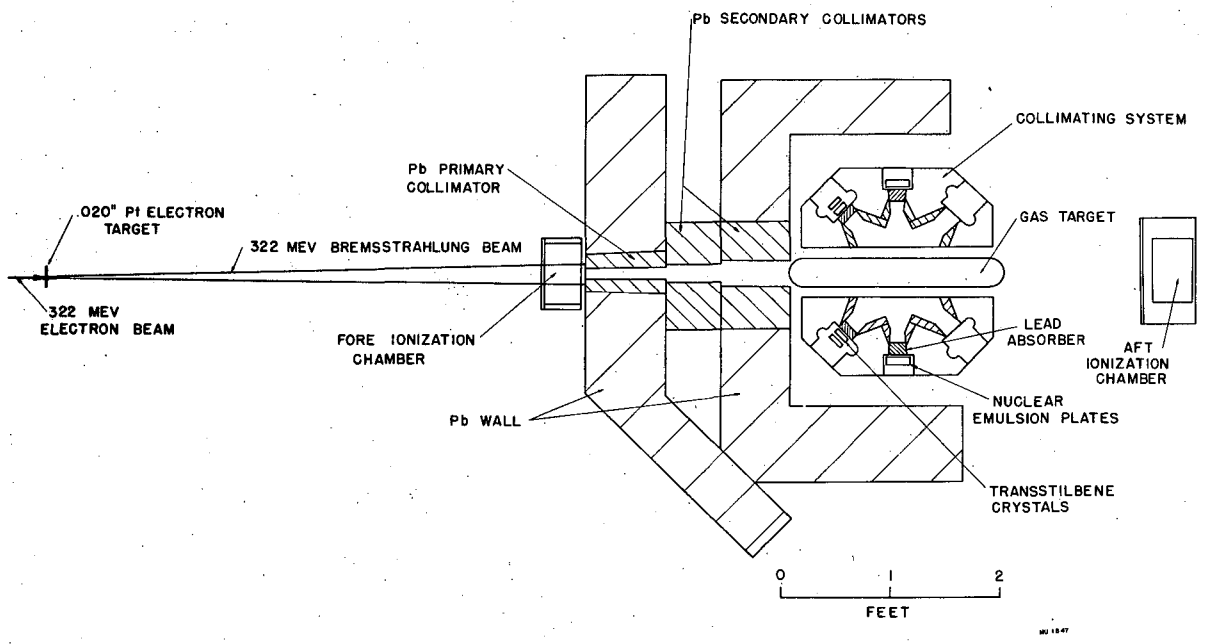
Pb SECONDARY COLLIMATORS
COLLIMATING SYSTEM
Pb PRIMARY COLLIMATOR
.020" Pt ELECTRON TARGET
322 MEV BREMSSTRAHLUNG BEAM
GAS TARGET
322 MEV ELECTRON BEAM
FORE IONIZATION CHAMBER
LEAD ABSORBER
AFT IONIZATION CHAMBER
Pb WALL
NUCLEAR EMULSION PLATES
TRANSSTILBENE CRYSTALS
0
1
2
FEET

Fig. 1

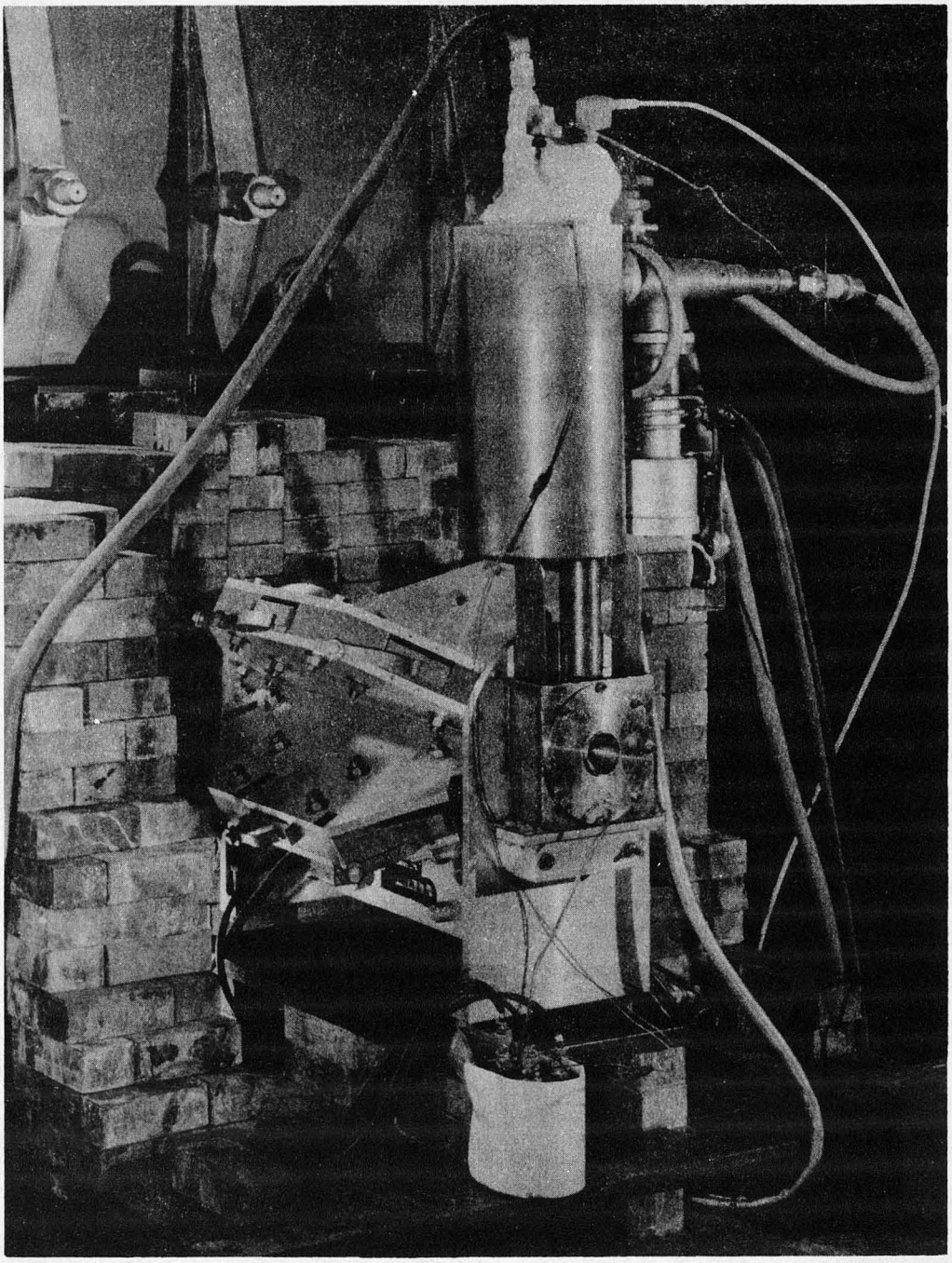

FIG. 2

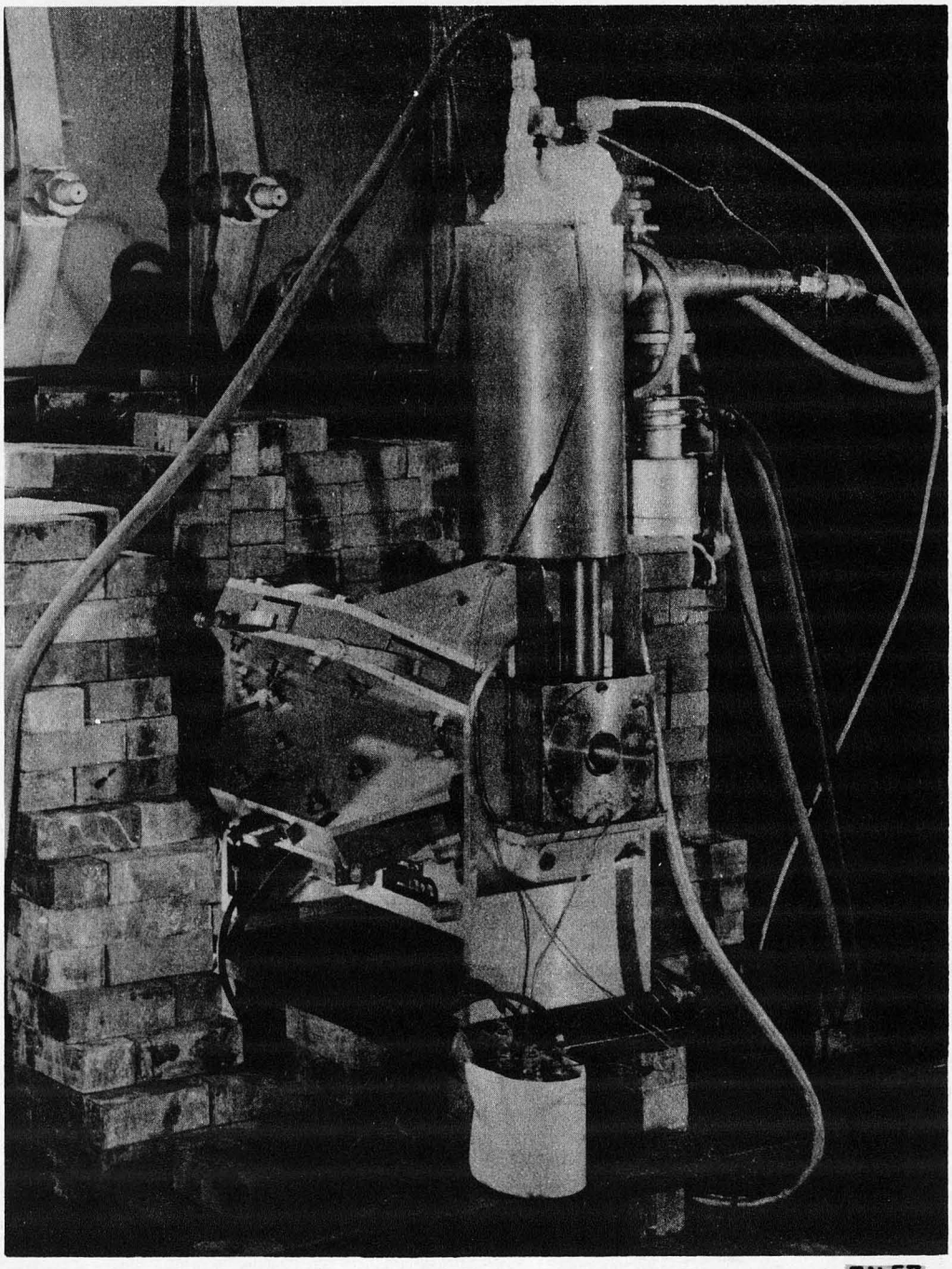

FIG. 2

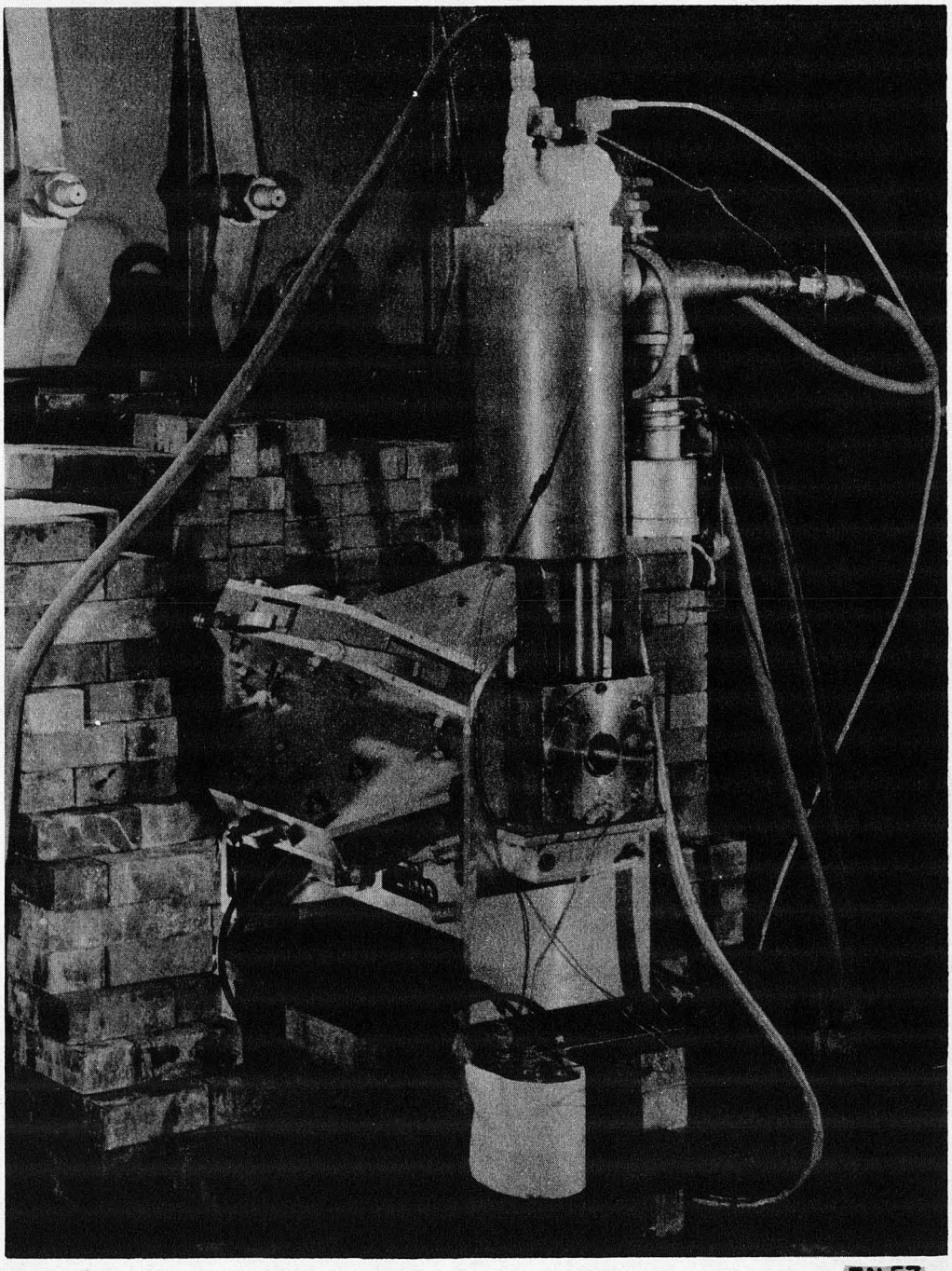

FIG. 2

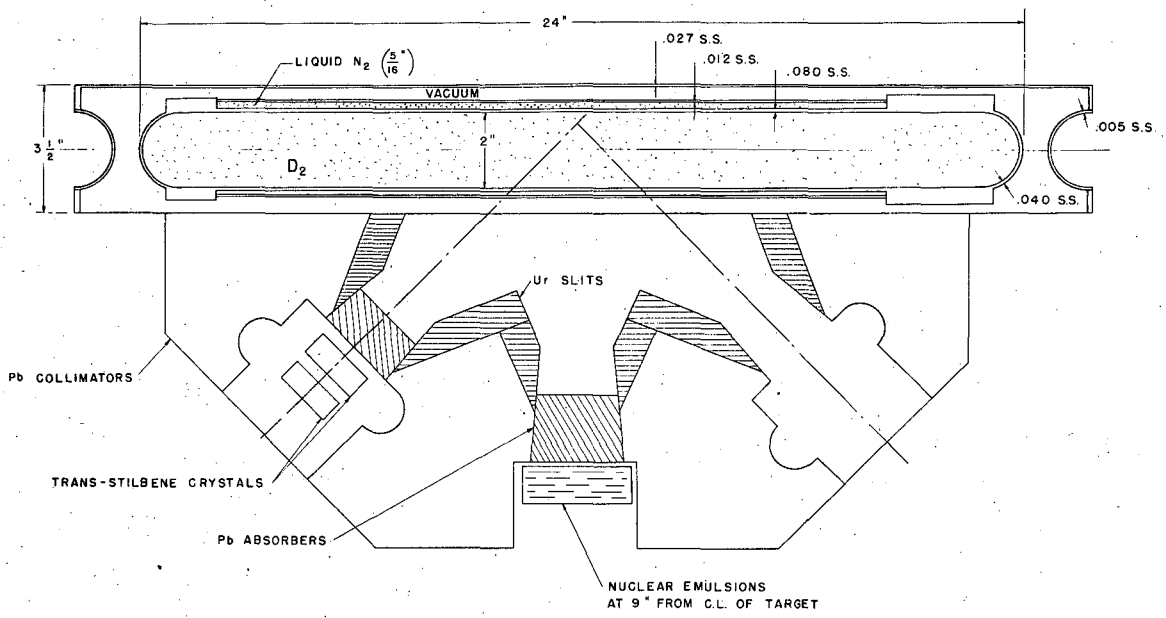
24"
.027 S.S.
.012 S.S.
.080 S.S.
LIQUID N_2 ($\frac{5}{16}$")
VACUUM
.005 S.S.
$3\frac{1}{2}$"
2"
D_2
.040 S.S.
Ur SLITS
Pb COLLIMATORS
TRANS-STILBENE CRYSTALS
Pb ABSORBERS
NUCLEAR EMULSIONS
AT 9" FROM C.L. OF TARGET
MU 1499

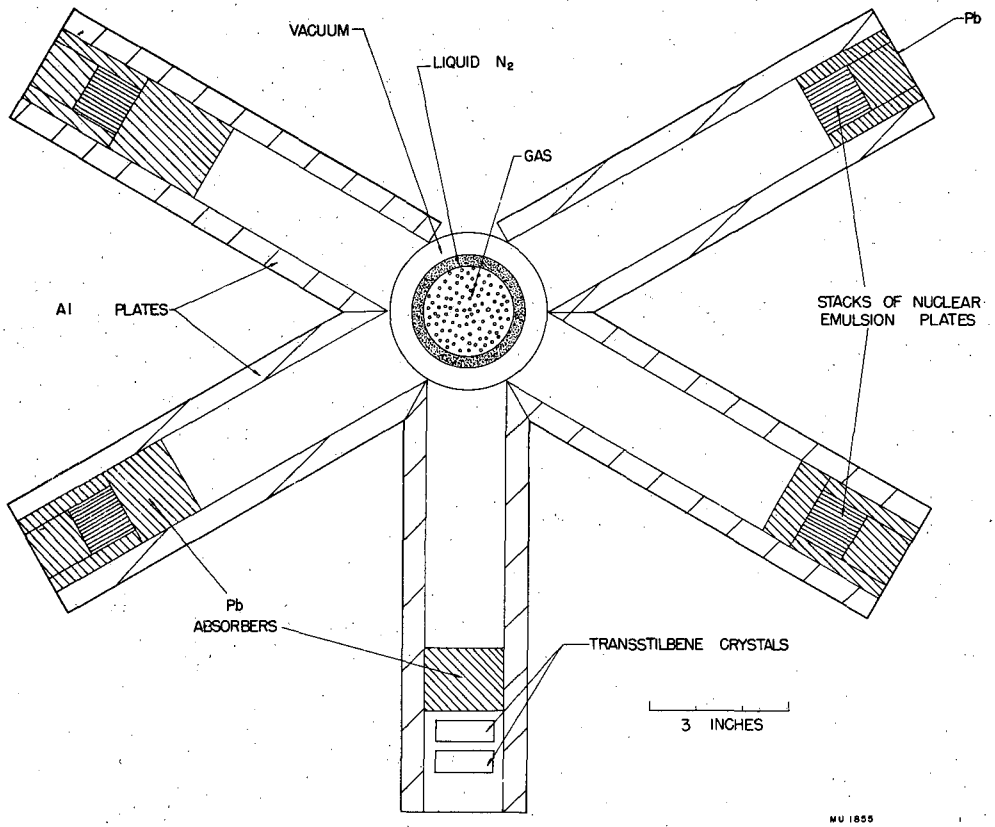
VACUUM
LIQUID N_2
GAS
Pb
Al PLATES
STACKS OF NUCLEAR
EMULSION PLATES
Pb
ABSORBERS
TRANSSTILBENE CRYSTALS
3 INCHES
MU 1855

Fig. 3

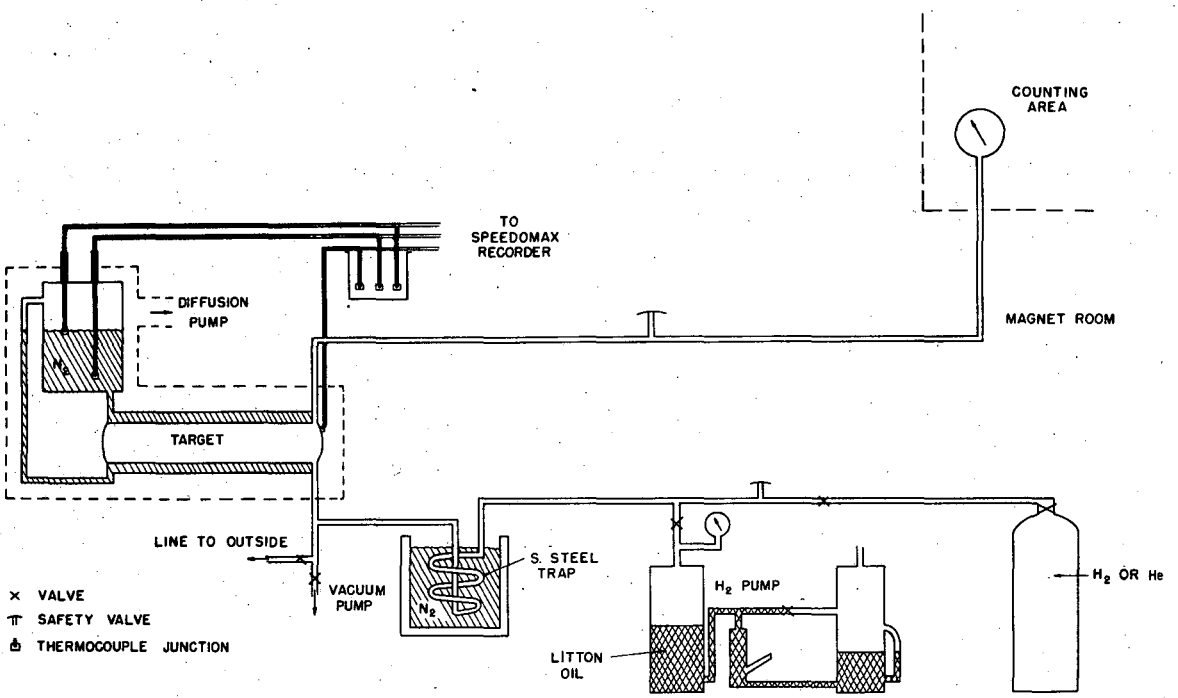

SCHEMATIC OF HIGH PRESSURE SYSTEM

Fig. 4

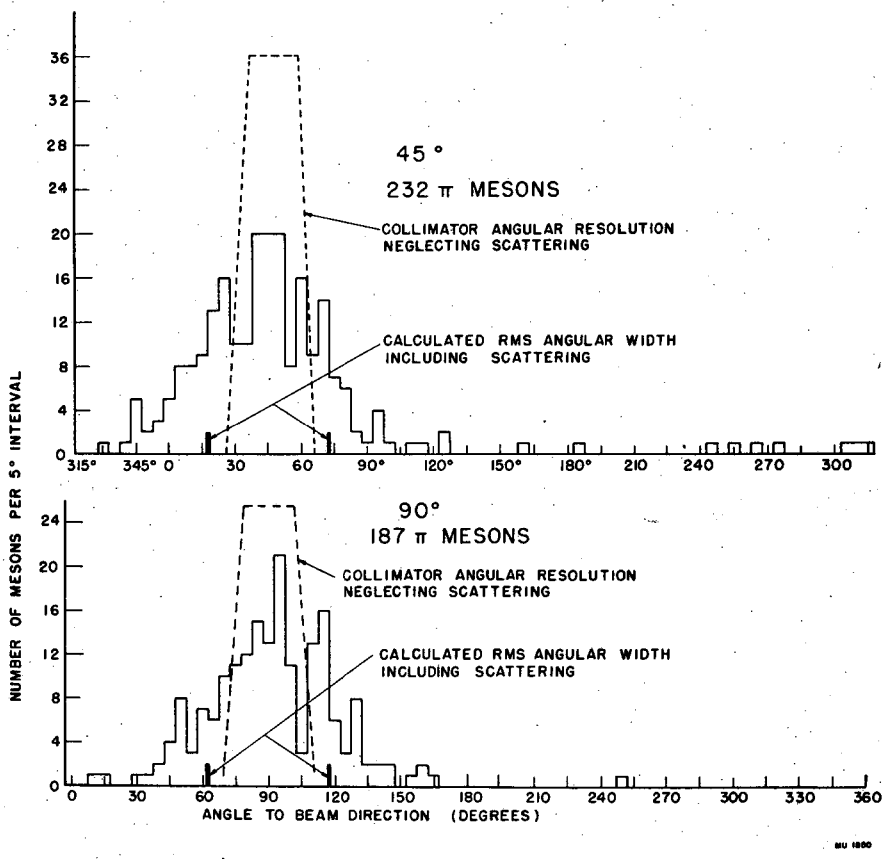
45°
232 π MESONS
COLLIMATOR ANGULAR RESOLUTION
NEGLECTING SCATTERING
CALCULATED RMS ANGULAR WIDTH
INCLUDING SCATTERING
90°
187 π MESONS
COLLIMATOR ANGULAR RESOLUTION
NEGLECTING SCATTERING
CALCULATED RMS ANGULAR WIDTH
INCLUDING SCATTERING
NUMBER OF MESONS PER 5° INTERVAL
ANGLE TO BEAM DIRECTION (DEGREES)

Fig. 5

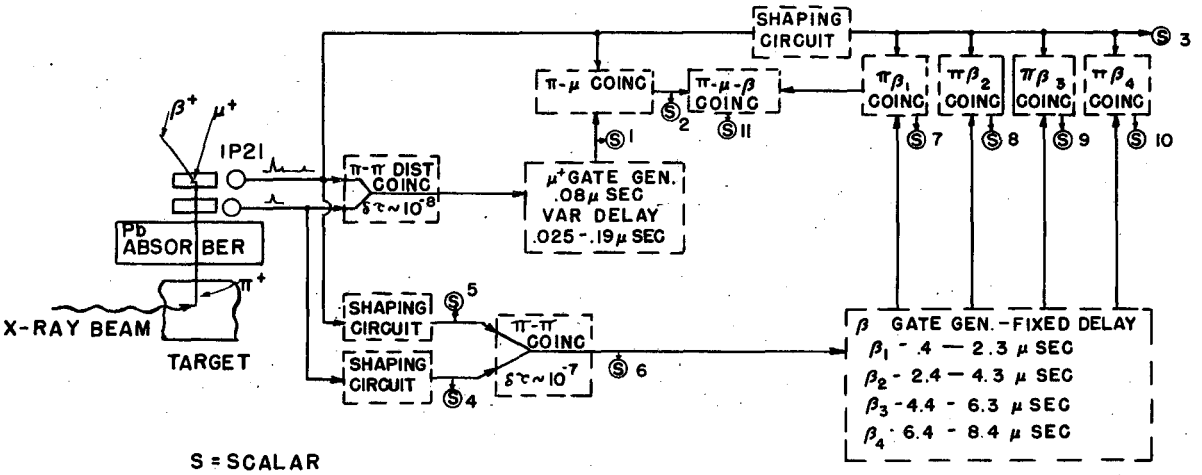

BLOCK DIAGRAM - ELECTRONICS

MU 1864

Fig. 7

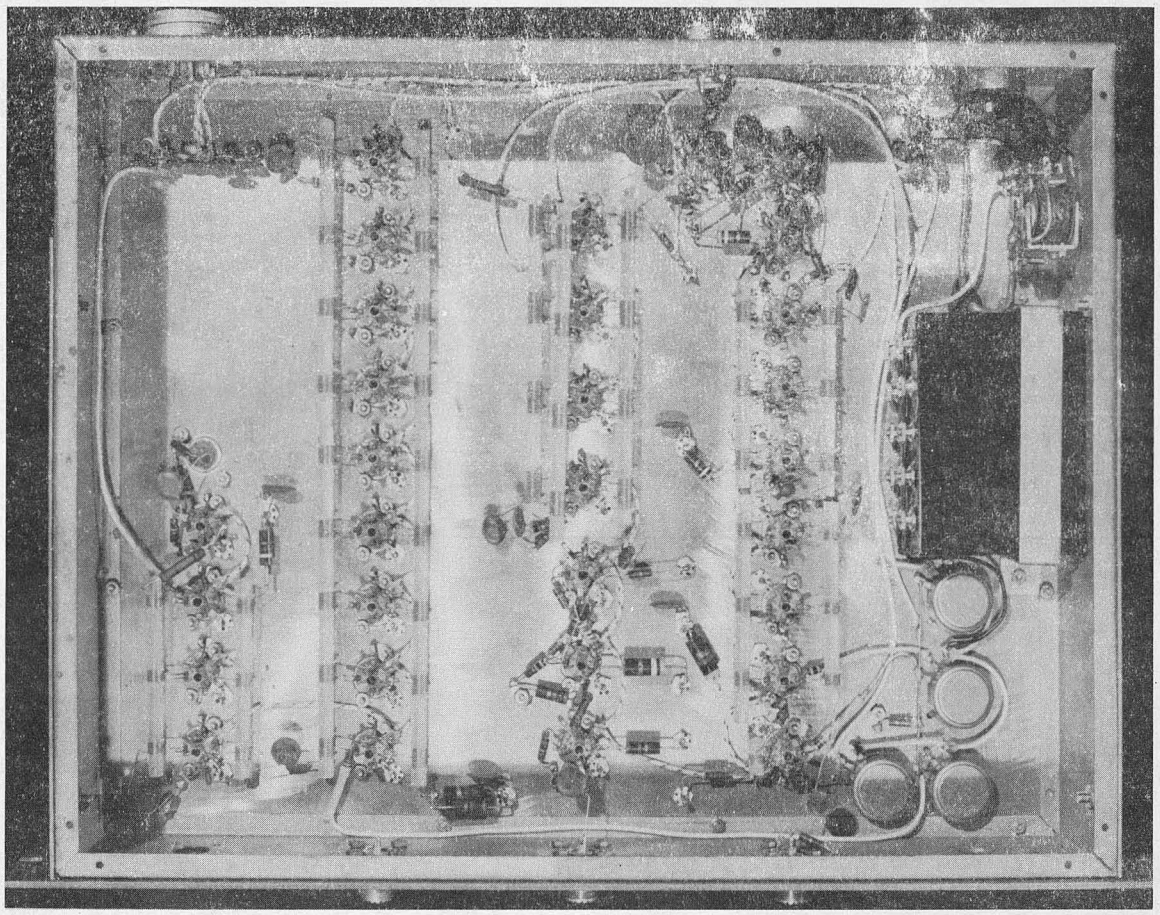

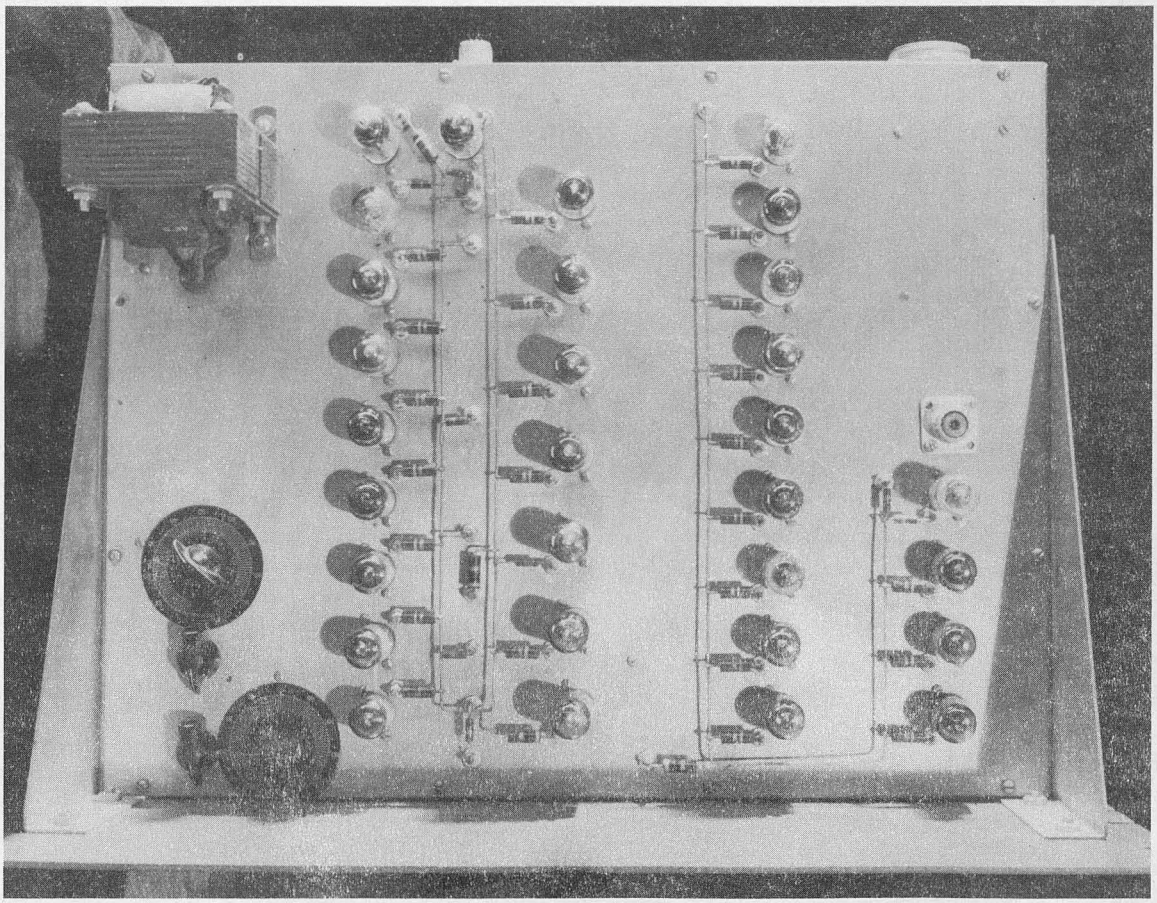

ZN 58

FIG. 8

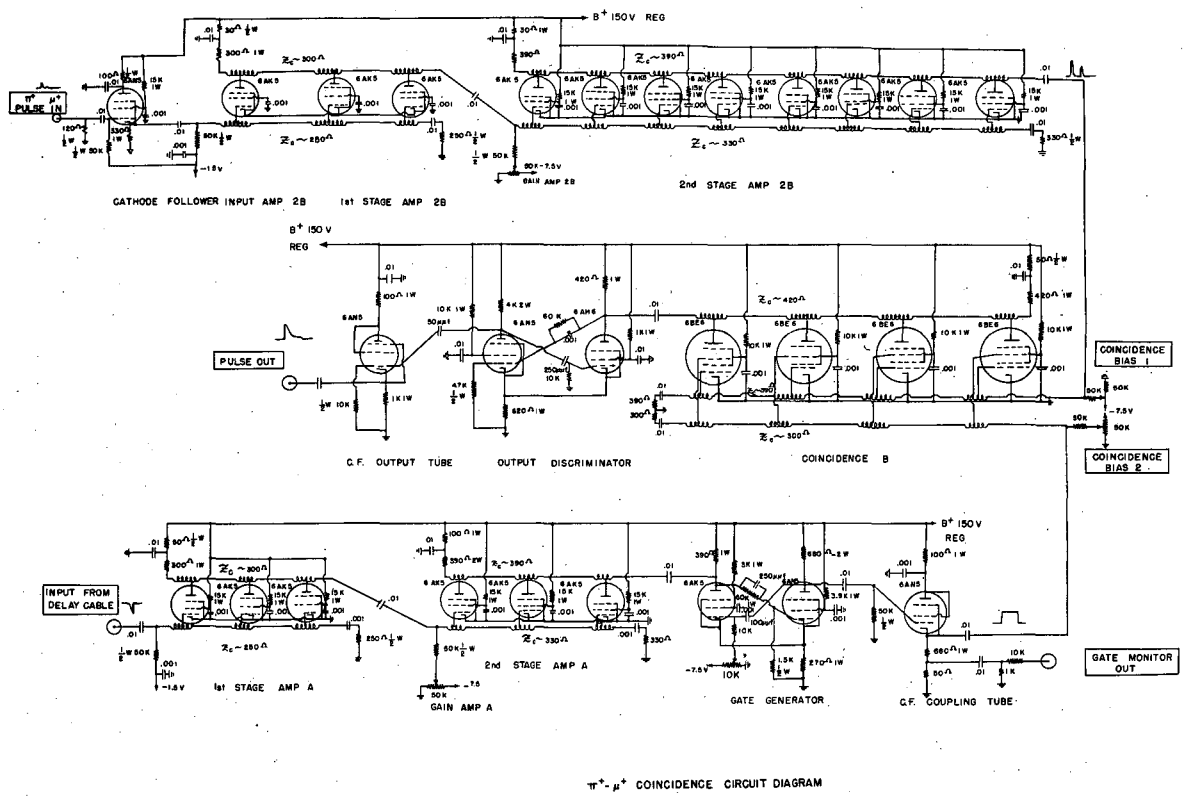
B+ 150V REG
π+ μ+ PULSE IN
CATHODE FOLLOWER INPUT AMP 2B
1st STAGE AMP 2B
GAIN AMP 2B
2nd STAGE AMP 2B
B+ 150 V REG
PULSE OUT
C.F. OUTPUT TUBE
OUTPUT DISCRIMINATOR
COINCIDENCE B
COINCIDENCE BIAS 1
COINCIDENCE BIAS 2
INPUT FROM DELAY CABLE
1st STAGE AMP A
2nd STAGE AMP A
GAIN AMP A
GATE GENERATOR
C.F. COUPLING TUBE
GATE MONITOR OUT
B+ 150V REG
π+-μ+ COINCIDENCE CIRCUIT DIAGRAM
MU 1918

Fig. 9

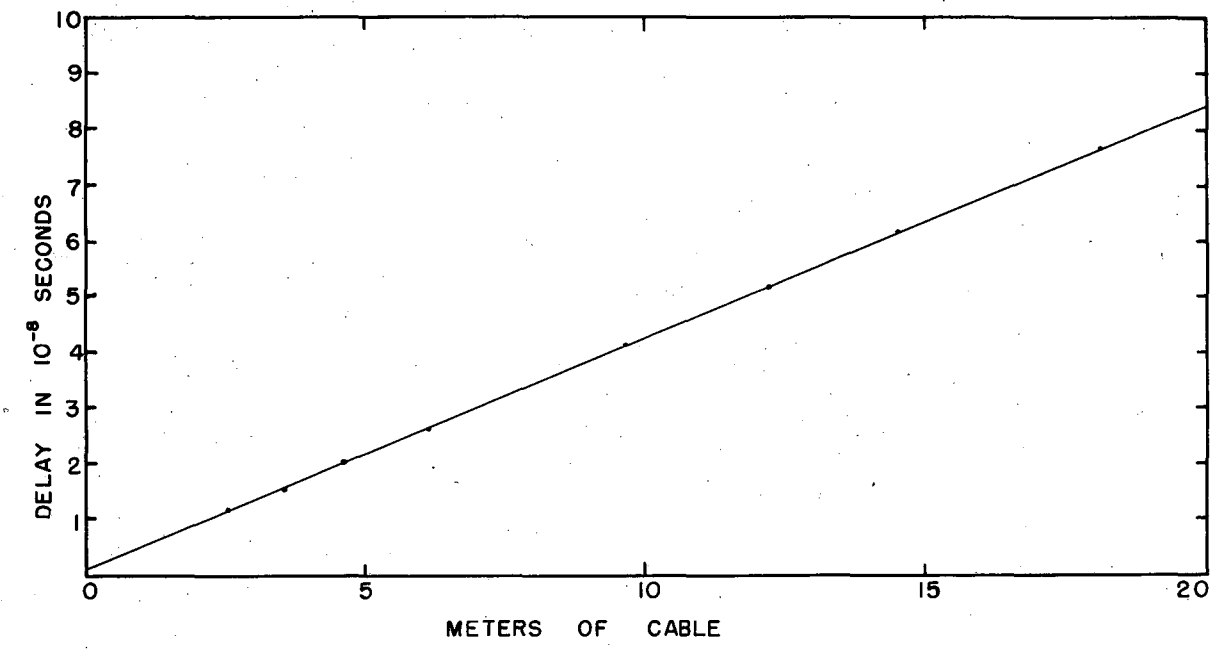

FIG. 4

DELAY IN RG 63/u CABLE

MU 1238

Fig. 10

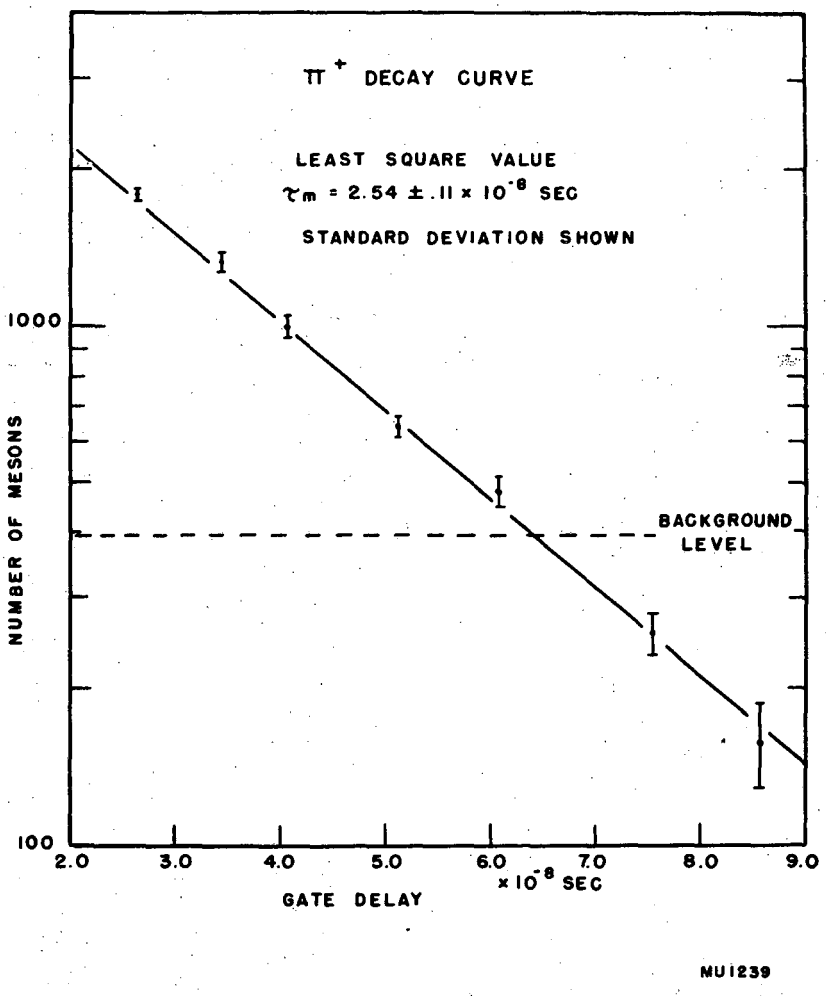
π⁺ DECAY CURVE
LEAST SQUARE VALUE
τm = 2.54 ± .11 x 10⁻⁸ SEC
STANDARD DEVIATION SHOWN
1000
100
NUMBER OF MESONS
BACKGROUND LEVEL
2.0
3.0
4.0
5.0
6.0
7.0
8.0
9.0
x 10⁻⁸ SEC
GATE DELAY
MU1239

Fig. 11

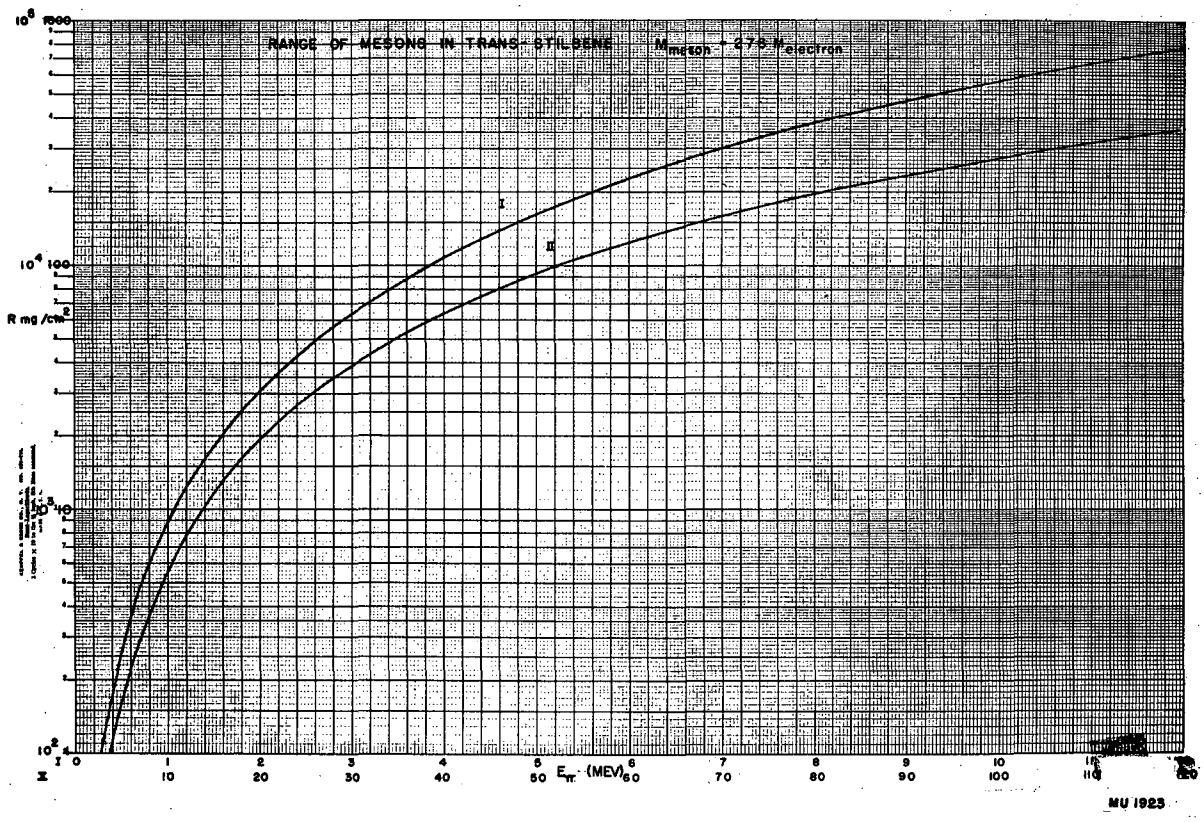
RANGE OF MESONS IN TRANS-STILBENE M meson = 279 M electron
R mg/cm²
E_π (MEV)
I
II
MU 1925

Fig. 13

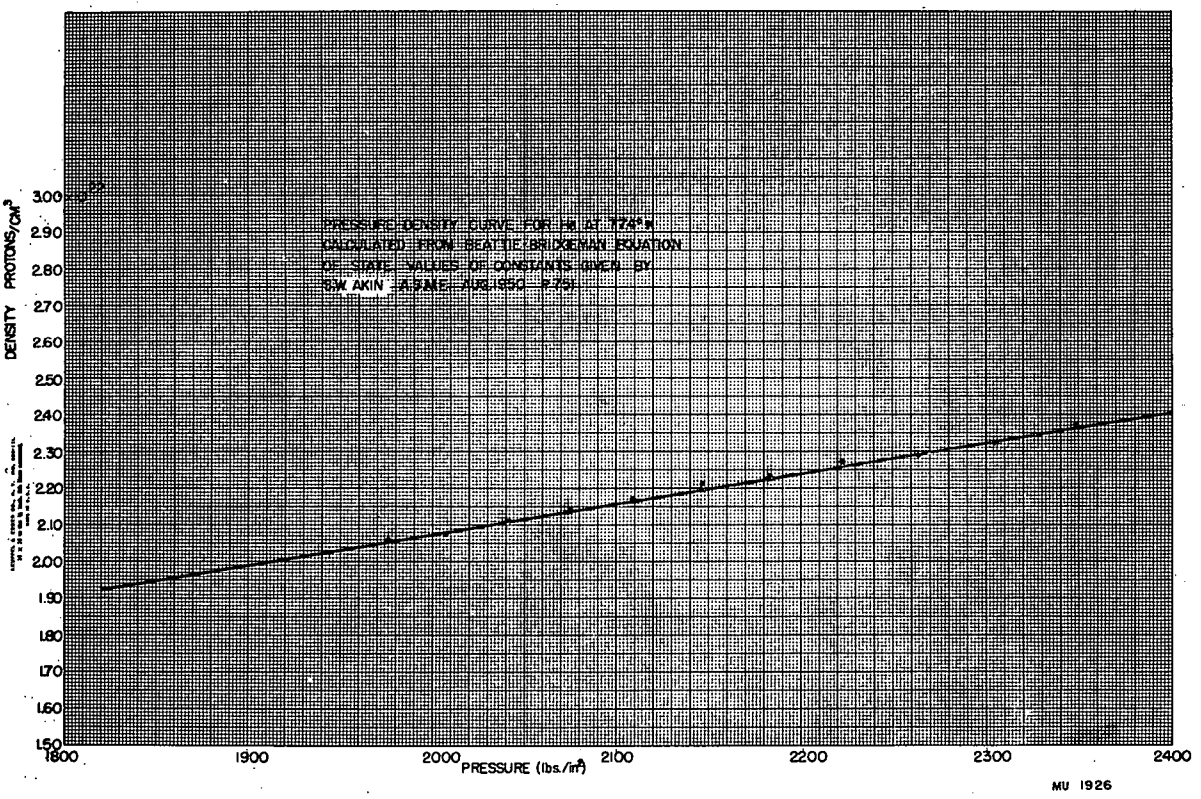
PRESSURE-DENSITY CURVE FOR H2 AT 77.4°K
CALCULATED FROM SEATTLE BRIDGEMAN EQUATION
OF STATE. VALUES OF CONSTANTS GIVEN BY
G.W. AKIN A.I.Ch.E. AUG.1950 P.751
DENSITY PROTONS/CM³
3.00 E22
2.90
2.80
2.70
2.60
2.50
2.40
2.30
2.20
2.10
2.00
1.90
1.80
1.70
1.60
1.50
1800
1900
2000
2100
2200
2300
2400
PRESSURE (lbs./in²)
MU 1926

Fig. 14

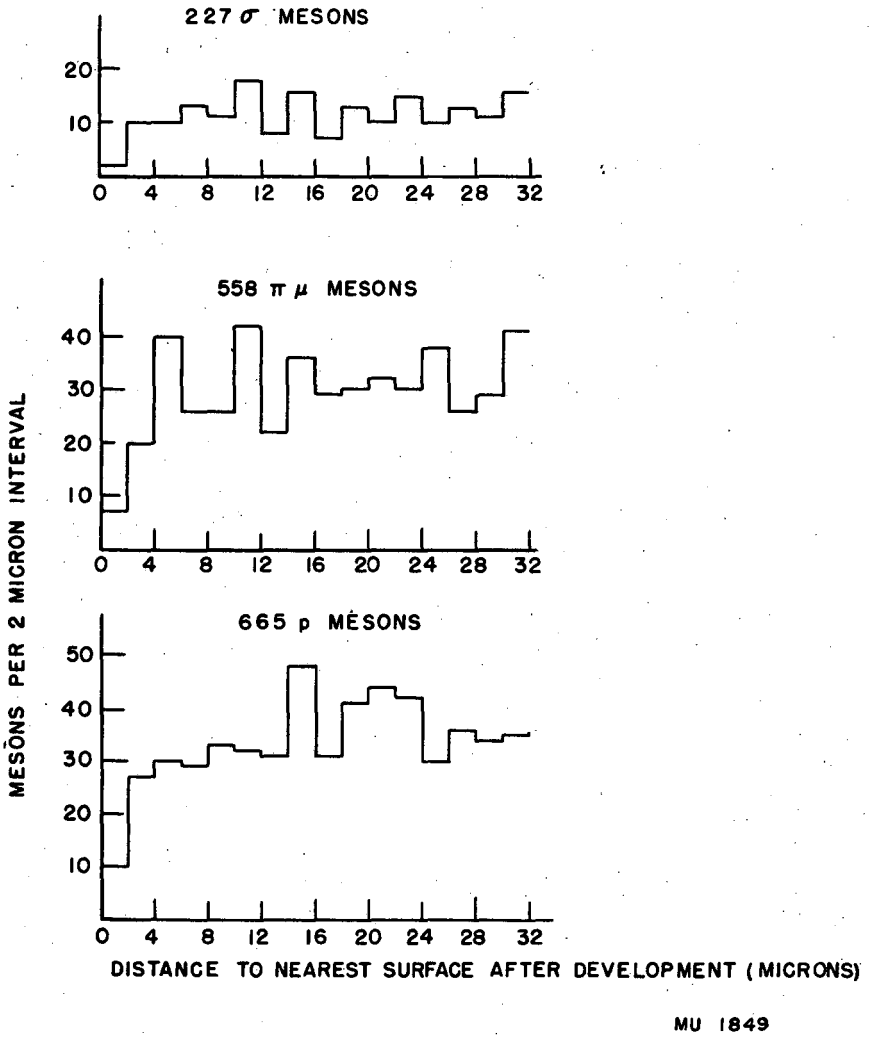
227 σ MESONS
558 π μ MESONS
665 p MESONS
MESONS PER 2 MICRON INTERVAL
DISTANCE TO NEAREST SURFACE AFTER DEVELOPMENT (MICRONS)
MU 1849

Fig. 15

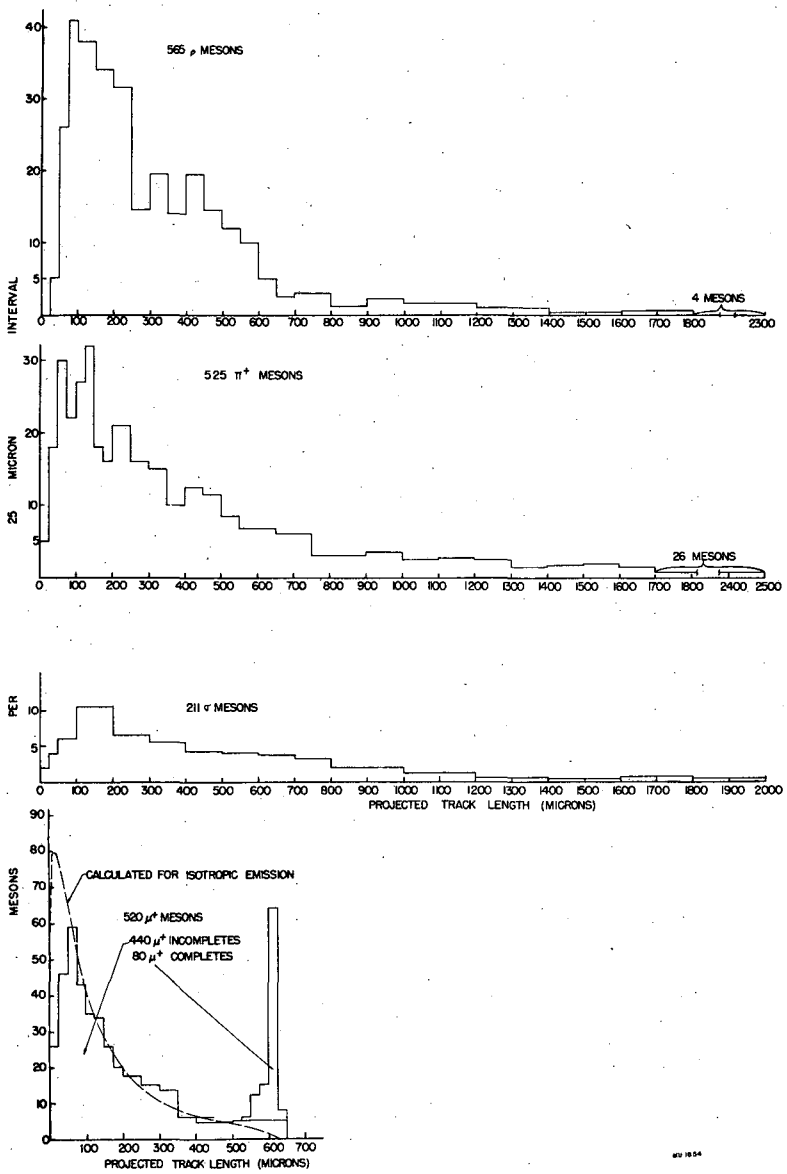
565 ρ MESONS
4 MESONS
INTERVAL
525 π+ MESONS
26 MESONS
MICRON
25
211 σ MESONS
PER
PROJECTED TRACK LENGTH (MICRONS)
CALCULATED FOR ISOTROPIC EMISSION
520 μ+ MESONS
440 μ+ INCOMPLETES
80 μ+ COMPLETES
MESONS
PROJECTED TRACK LENGTH (MICRONS)

Fig. 16

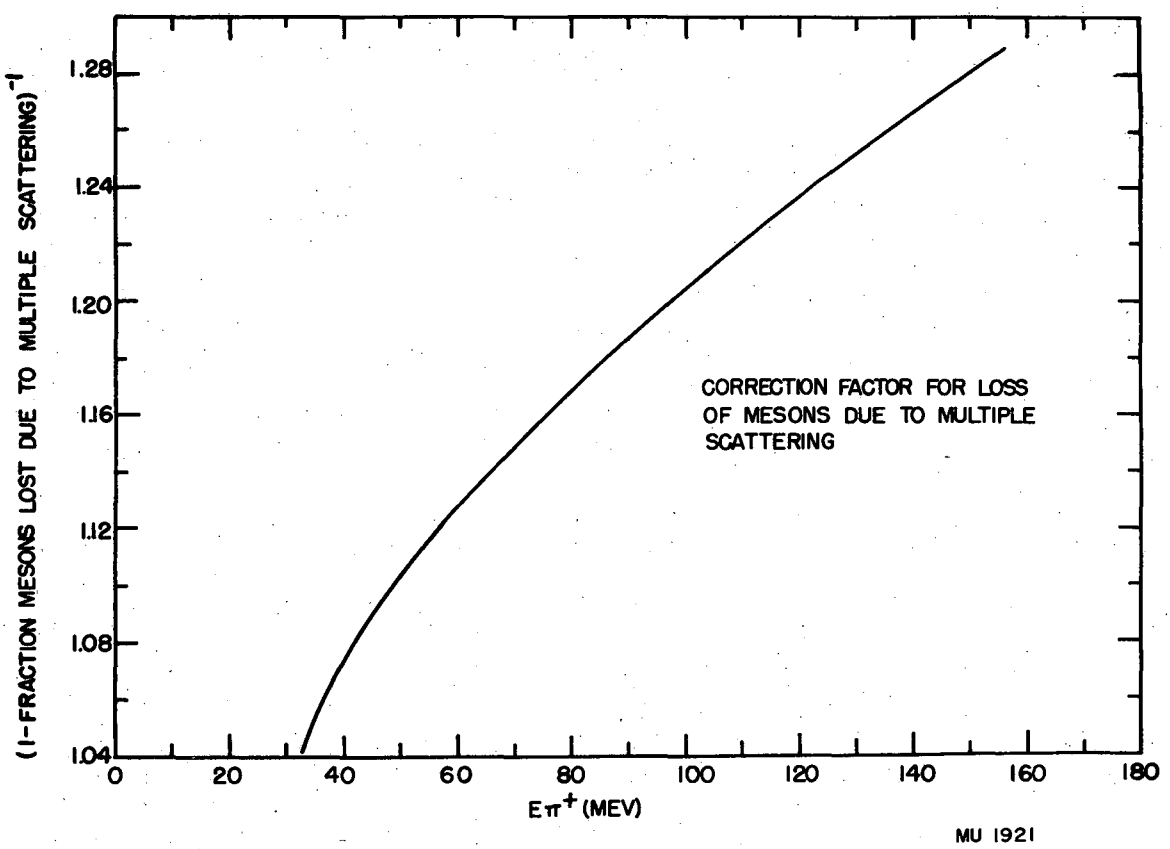
(1-FRACTION MESONS LOST DUE TO MULTIPLE SCATTERING)$^{-1}$
1.28
1.24
1.20
1.16
1.12
1.08
1.04
0
20
40
60
80
100
120
140
160
180
$E\pi^+$ (MEV)
CORRECTION FACTOR FOR LOSS OF MESONS DUE TO MULTIPLE SCATTERING
MU 1921

Fig. 17

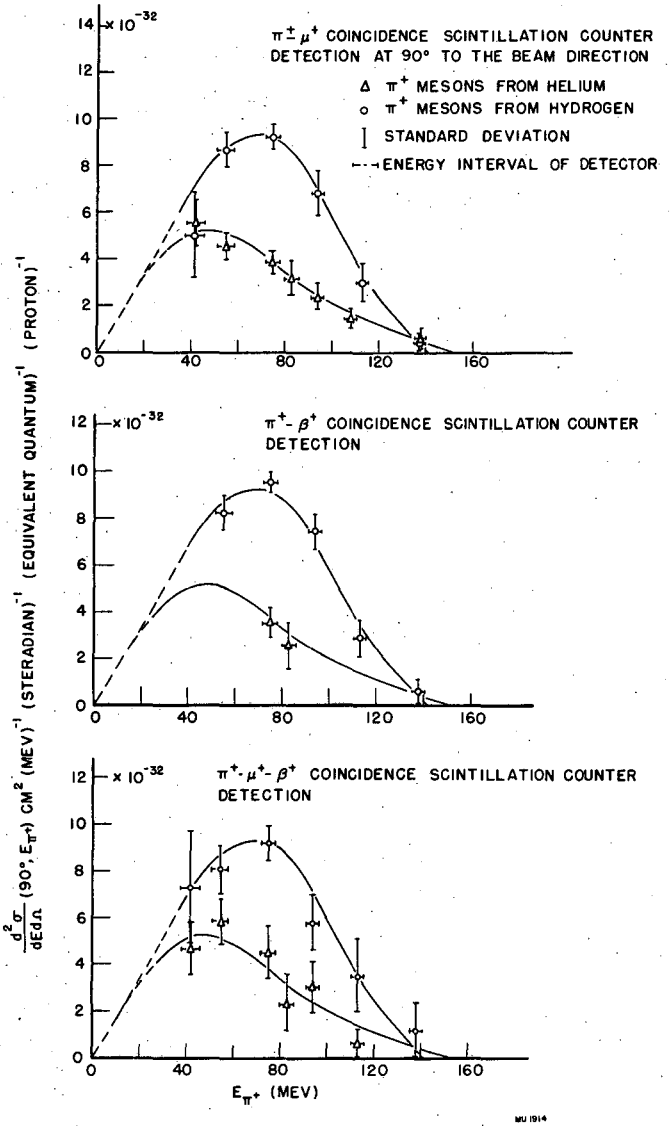
$\pi^{\pm}\mu^{+}$ COINCIDENCE SCINTILLATION COUNTER DETECTION AT 90° TO THE BEAM DIRECTION
Δ π^{+} MESONS FROM HELIUM
o π^{+} MESONS FROM HYDROGEN
STANDARD DEVIATION
ENERGY INTERVAL OF DETECTOR
π^{+}-β^{+} COINCIDENCE SCINTILLATION COUNTER DETECTION
π^{+}-μ^{+}-β^{+} COINCIDENCE SCINTILLATION COUNTER DETECTION
$\frac{d^2\sigma}{dEd\Omega}(90°, E_{\pi^+})$ CM^2 (MEV)$^{-1}$ (STERADIAN)$^{-1}$ (EQUIVALENT QUANTUM)$^{-1}$ (PROTON)$^{-1}$
E_{π^+} (MEV)
MU 1914

Fig. 18

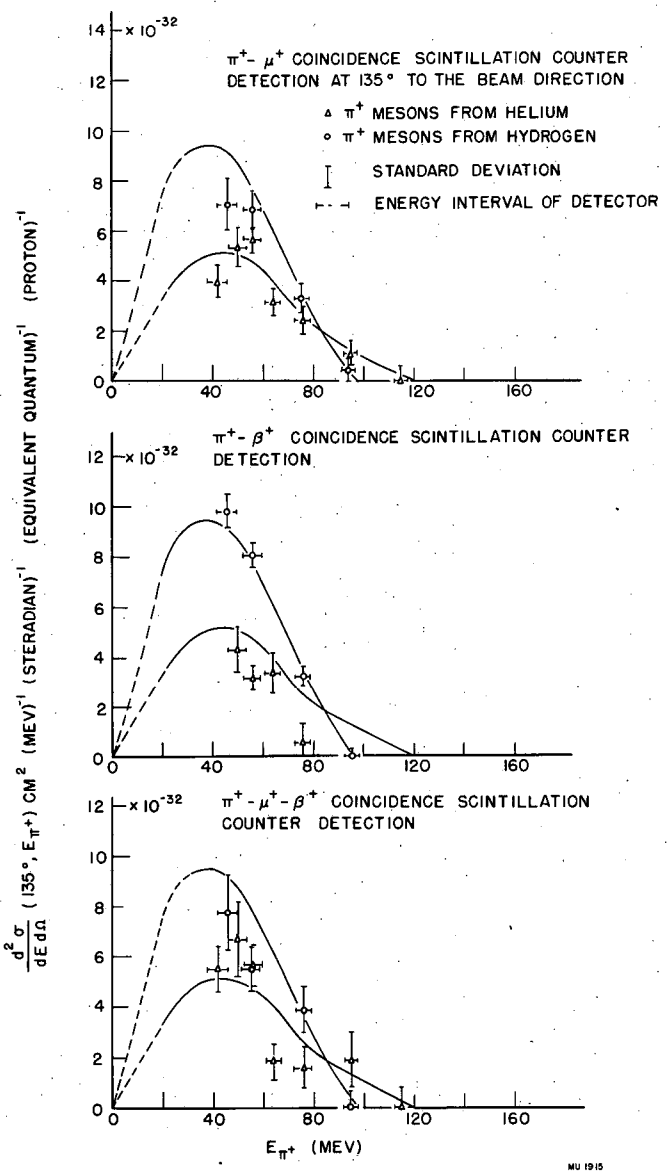
$\pi^+ - \mu^+$ COINCIDENCE SCINTILLATION COUNTER
DETECTION AT 135° TO THE BEAM DIRECTION
π^+ MESONS FROM HELIUM
π^+ MESONS FROM HYDROGEN
STANDARD DEVIATION
ENERGY INTERVAL OF DETECTOR
$\pi^+ - \beta^+$ COINCIDENCE SCINTILLATION COUNTER
DETECTION
$\pi^+ - \mu^+ - \beta^+$ COINCIDENCE SCINTILLATION
COUNTER DETECTION
$\frac{d^2\sigma}{dE\,d\Omega}$ (135°, E_{π^+}) CM^2 (MEV)$^{-1}$ (STERADIAN)$^{-1}$ (EQUIVALENT QUANTUM)$^{-1}$ (PROTON)$^{-1}$
E_{π^+} (MEV)
MU 1915

Fig. 19

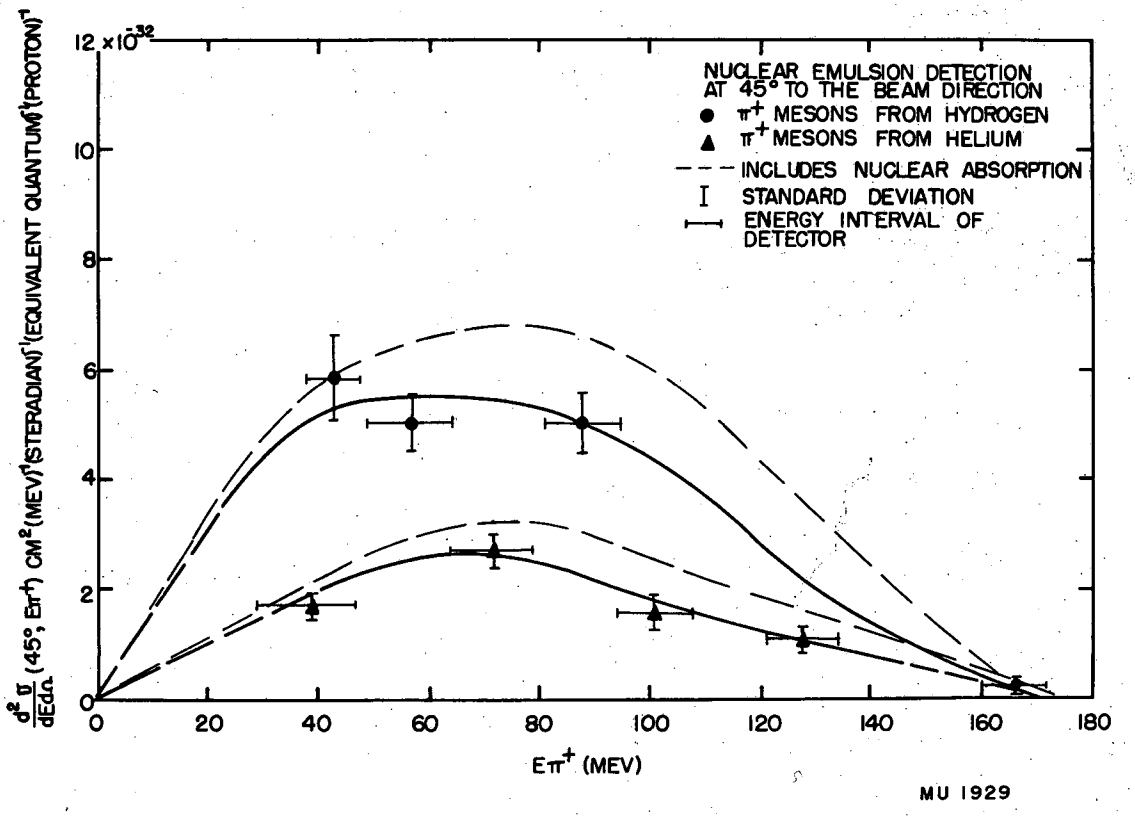
NUCLEAR EMULSION DETECTION
AT 45° TO THE BEAM DIRECTION
π+ MESONS FROM HYDROGEN
π+ MESONS FROM HELIUM
INCLUDES NUCLEAR ABSORPTION
STANDARD DEVIATION
ENERGY INTERVAL OF DETECTOR
12 x10-32
10
8
6
4
2
0
0
20
40
60
80
100
120
140
160
180
Eπ+ (MEV)
MU 1929

Fig. 20

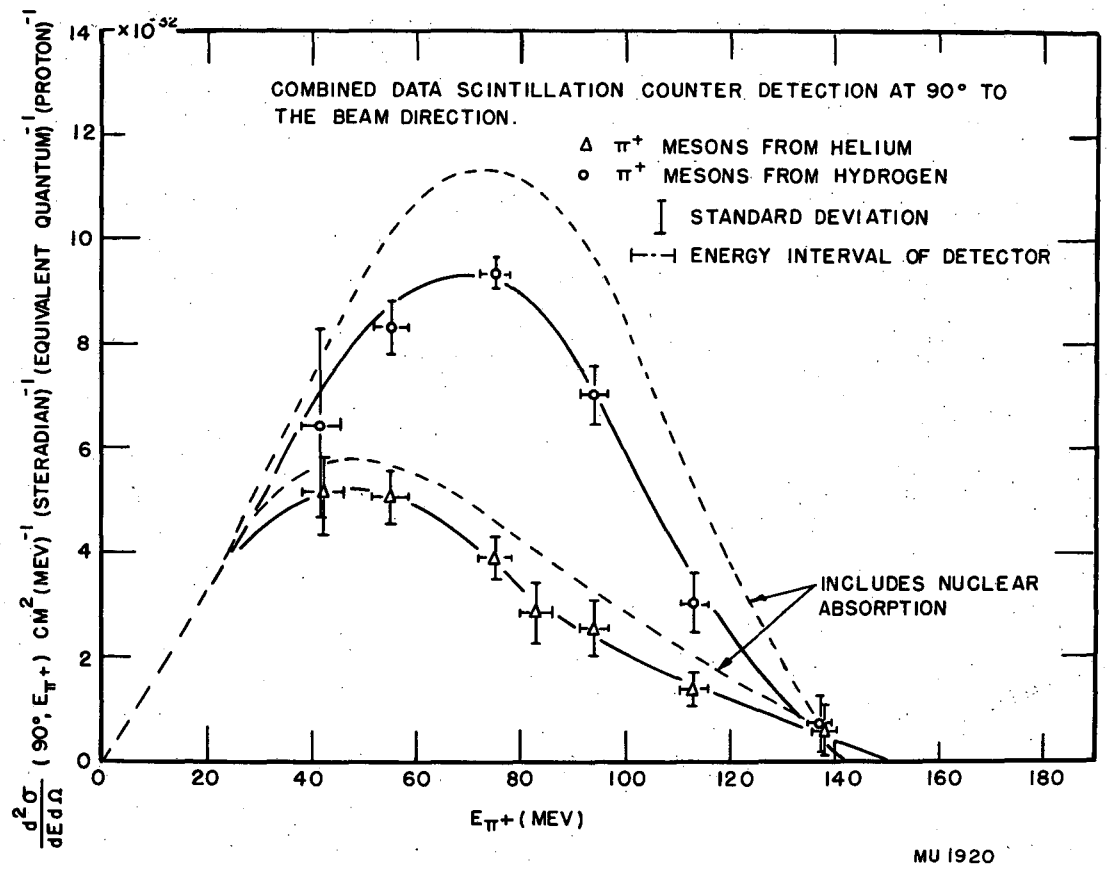
COMBINED DATA SCINTILLATION COUNTER DETECTION AT 90° TO THE BEAM DIRECTION.
Δ π+ MESONS FROM HELIUM
o π+ MESONS FROM HYDROGEN
STANDARD DEVIATION
ENERGY INTERVAL OF DETECTOR
INCLUDES NUCLEAR ABSORPTION
×10⁻³²
$\frac{d^2\sigma}{dEd\Omega}$ (90°, E_{π^+}) CM² (MEV)⁻¹ (STERADIAN)⁻¹ (EQUIVALENT QUANTUM)⁻¹ (PROTON)⁻¹
E_{π^+} (MEV)
0
2
4
6
8
10
12
14
0
20
40
60
80
100
120
140
160
180
MU 1920

Fig. 21

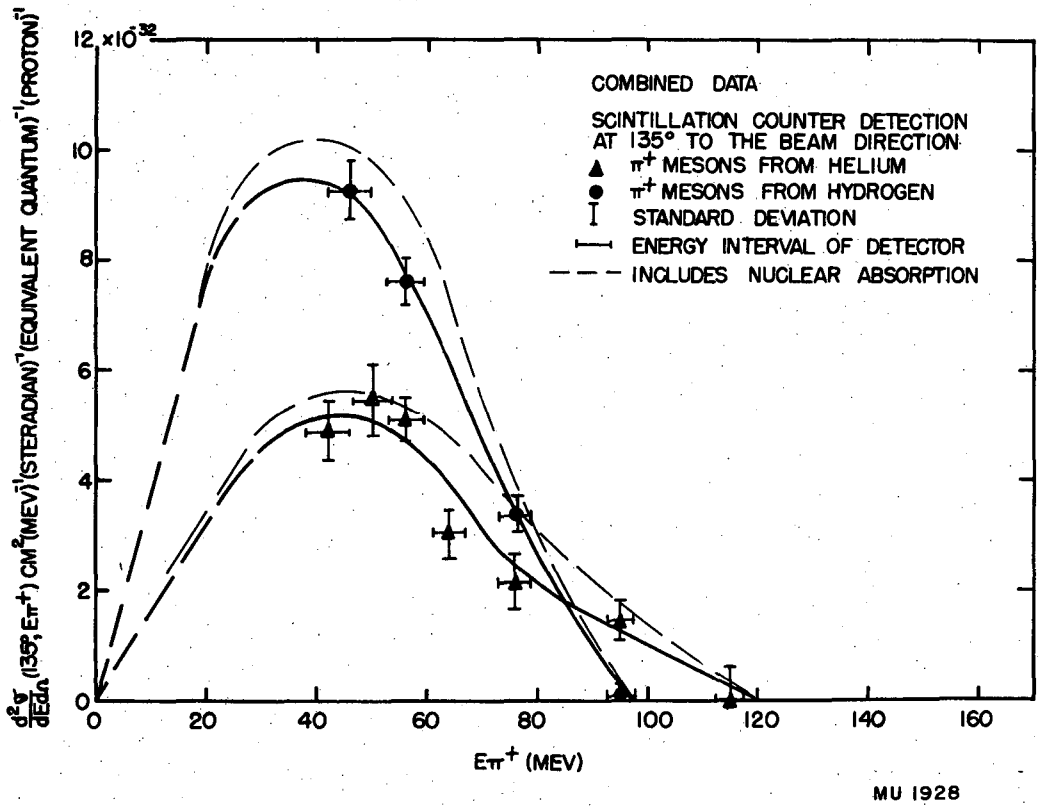
12 x10⁻³²
10
8
6
4
2
0
0
20
40
60
80
100
120
140
160
Eπ⁺ (MEV)
COMBINED DATA
SCINTILLATION COUNTER DETECTION AT 135° TO THE BEAM DIRECTION
π⁺ MESONS FROM HELIUM
π⁺ MESONS FROM HYDROGEN
STANDARD DEVIATION
ENERGY INTERVAL OF DETECTOR
INCLUDES NUCLEAR ABSORPTION
MU 1928

Fig. 22

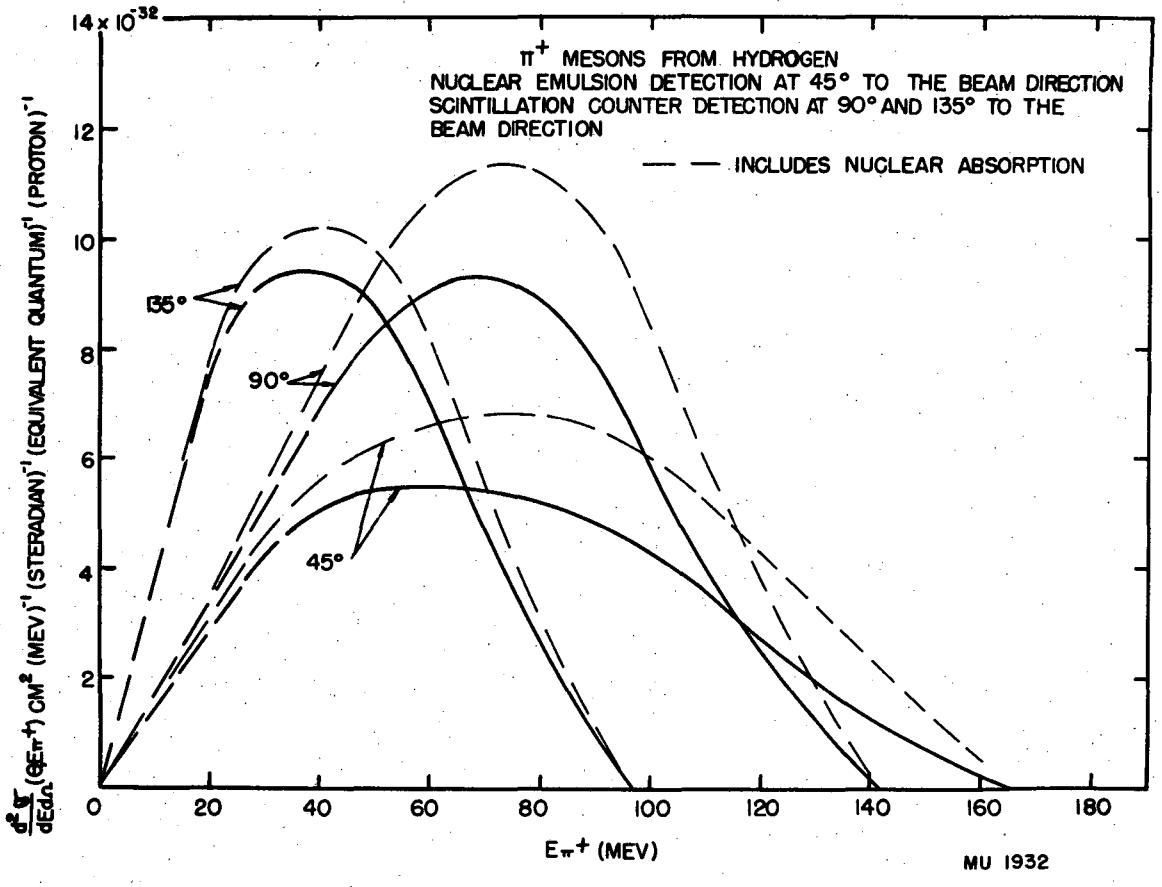
14 x 10⁻³²
π⁺ MESONS FROM HYDROGEN
NUCLEAR EMULSION DETECTION AT 45° TO THE BEAM DIRECTION
SCINTILLATION COUNTER DETECTION AT 90° AND 135° TO THE BEAM DIRECTION
— — INCLUDES NUCLEAR ABSORPTION
135°
90°
45°
12
10
8
6
4
2
0
20
40
60
80
100
120
140
160
180
Eπ+ (MEV)
MU 1932

Fig. 23

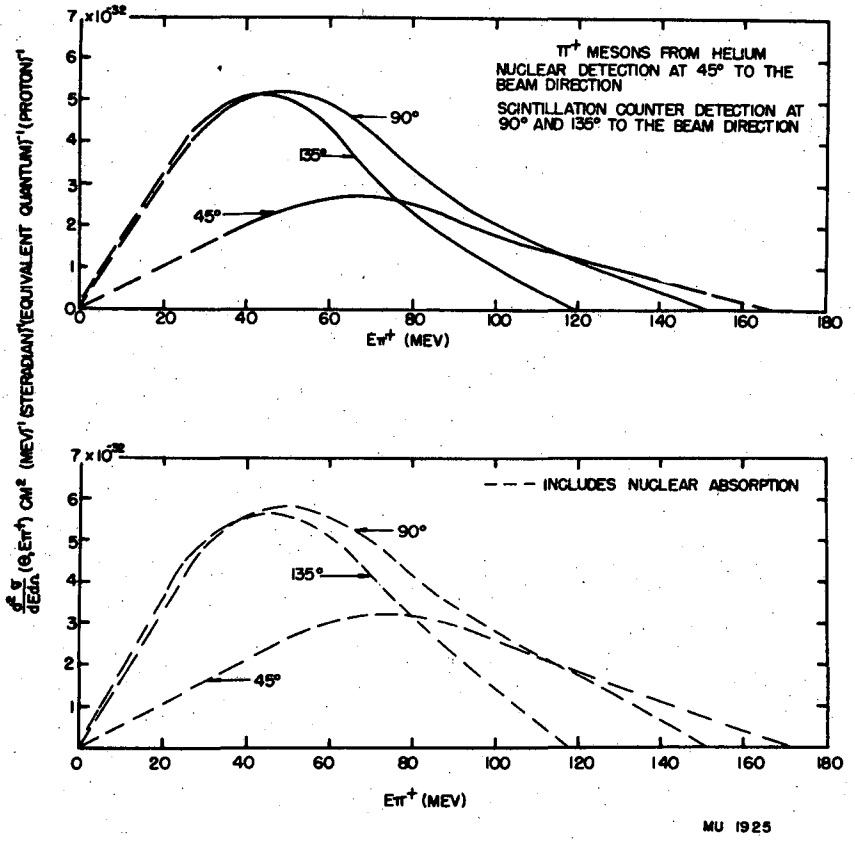
π^+ MESONS FROM HELIUM
NUCLEAR DETECTION AT 45° TO THE BEAM DIRECTION
SCINTILLATION COUNTER DETECTION AT 90° AND 135° TO THE BEAM DIRECTION
90°
135°
45°
INCLUDES NUCLEAR ABSORPTION
E_{π^+} (MEV)
$\frac{d^2\sigma}{dE d\Omega}(\theta, E_{\pi^+})$ CM^2 (MEV)$^{-1}$ (STERADIAN)$^{-1}$(EQUIVALENT QUANTUM)$^{-1}$(PROTON)$^{-1}$
MU 1925

Fig. 24

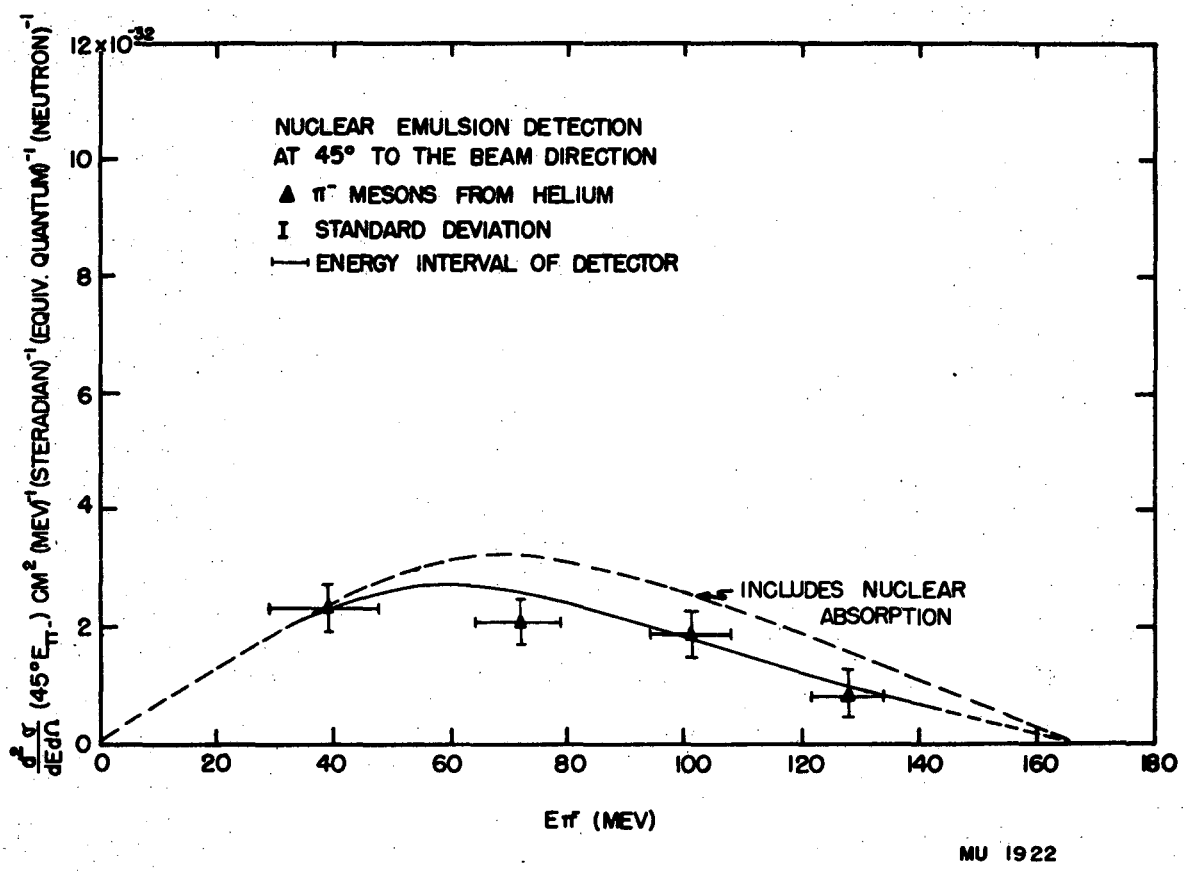
NUCLEAR EMULSION DETECTION
AT 45° TO THE BEAM DIRECTION
▲ π⁻ MESONS FROM HELIUM
I STANDARD DEVIATION
ENERGY INTERVAL OF DETECTOR
INCLUDES NUCLEAR ABSORPTION
$\frac{d^2\sigma}{dEd\Omega}(45°E_{\pi^-})$ CM² (MEV)⁻¹(STERADIAN)⁻¹(EQUIV. QUANTUM)⁻¹(NEUTRON)⁻¹
12×10⁻³²
10
8
6
4
2
0
0
20
40
60
80
100
120
140
160
180
Eπ⁻ (MEV)
MU 1922

Fig. 25

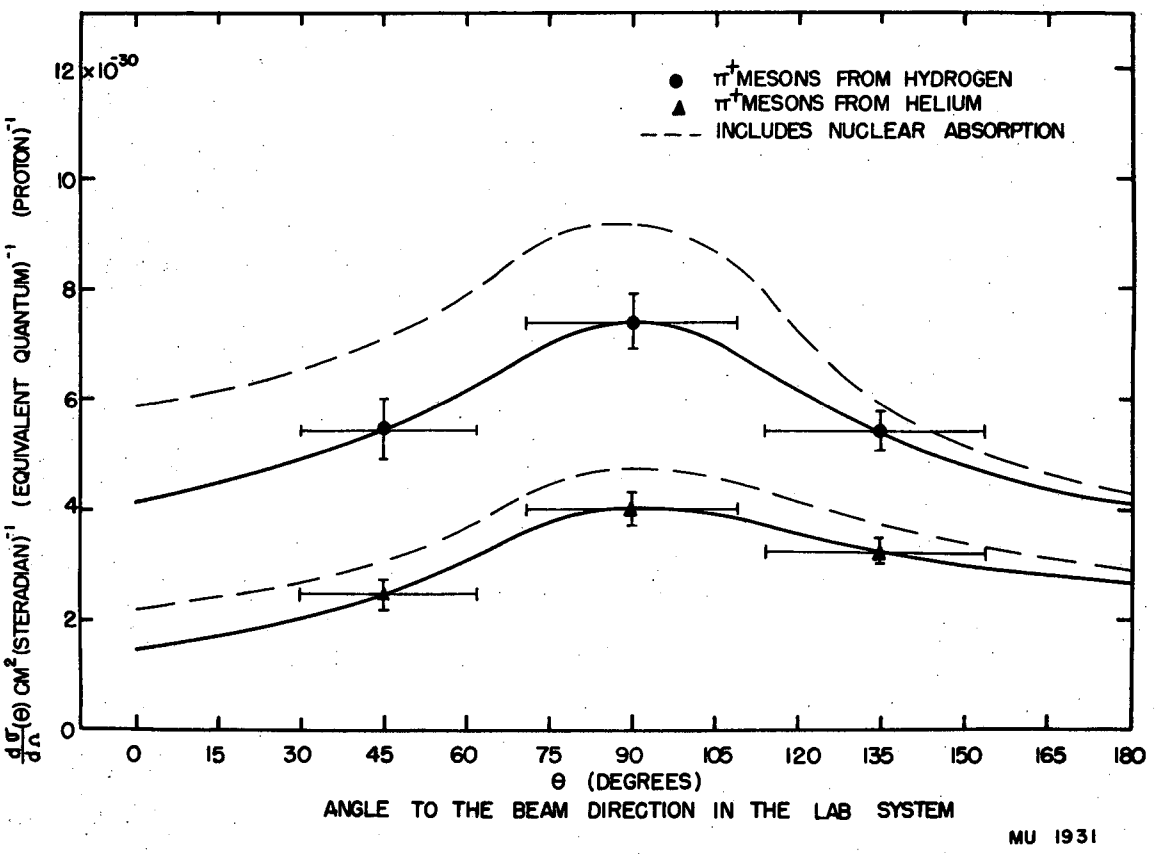
12 x 10⁻³⁰
10
8
6
4
2
0
π⁺MESONS FROM HYDROGEN
π⁺MESONS FROM HELIUM
INCLUDES NUCLEAR ABSORPTION
dσ/dΩ (θ) CM² (STERADIAN)⁻¹ (EQUIVALENT QUANTUM)⁻¹ (PROTON)⁻¹
0 15 30 45 60 75 90 105 120 135 150 165 180
θ (DEGREES)
ANGLE TO THE BEAM DIRECTION IN THE LAB SYSTEM
MU 1931

Fig. 26

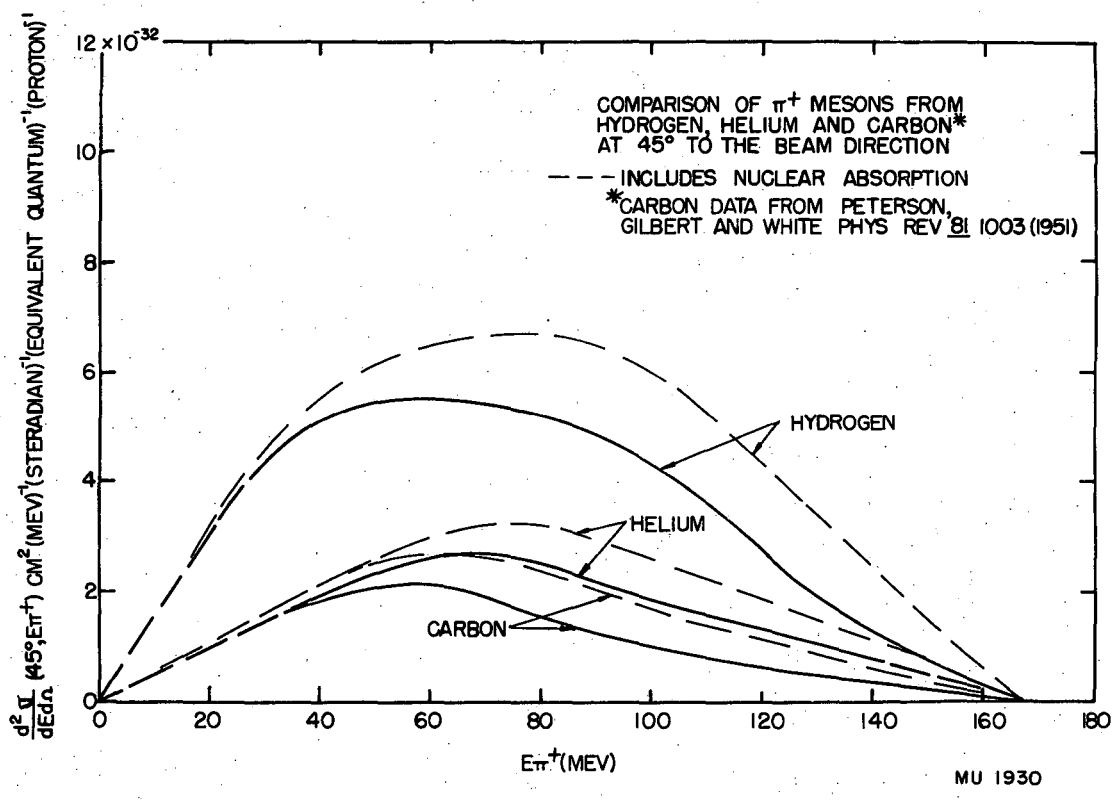
COMPARISON OF π+ MESONS FROM HYDROGEN, HELIUM AND CARBON* AT 45° TO THE BEAM DIRECTION
– – – INCLUDES NUCLEAR ABSORPTION
*CARBON DATA FROM PETERSON, GILBERT AND WHITE PHYS REV 81 1003 (1951)
HYDROGEN
HELIUM
CARBON
12 x 10^-32
10
8
6
4
2
0
0
20
40
60
80
100
120
140
160
180
Eπ+(MEV)
d²σ/dEdΩ (45°,Eπ+) CM²(MEV)⁻¹(STERADIAN)⁻¹(EQUIVALENT QUANTUM)⁻¹(PROTON)⁻¹
MU 1930

Fig. 27

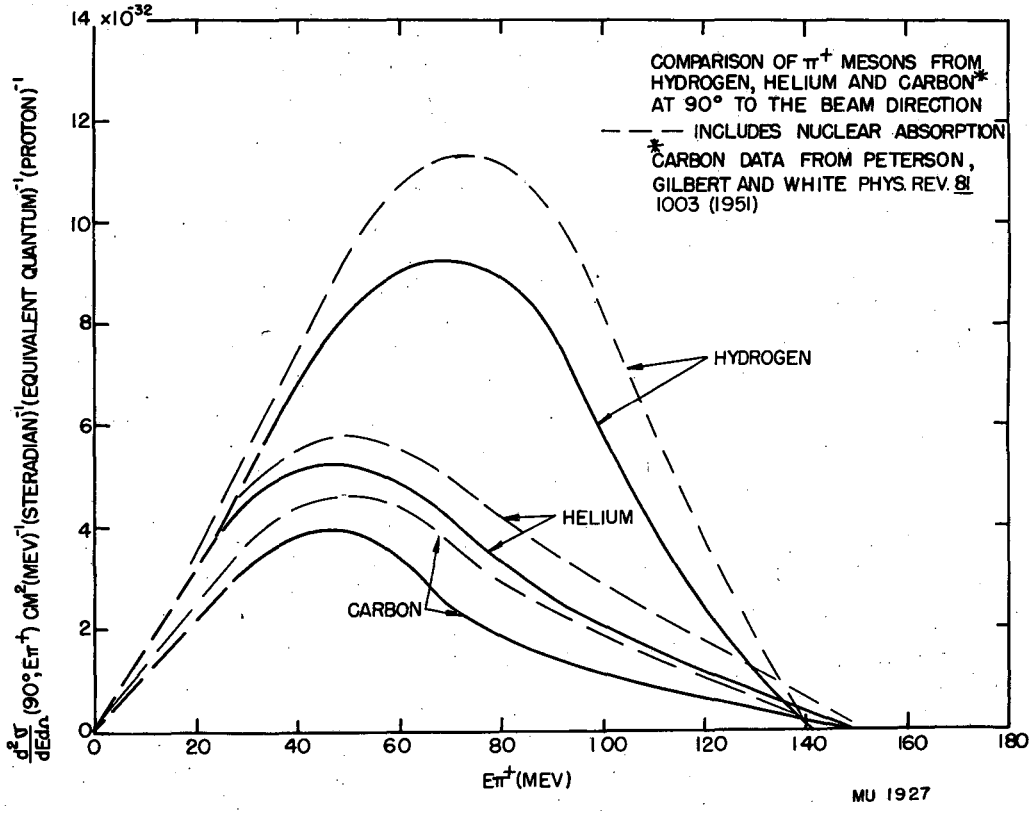
14 x10^-32
12
10
8
6
4
2
0
0
20
40
60
80
100
120
140
160
180
COMPARISON OF π+ MESONS FROM HYDROGEN, HELIUM AND CARBON* AT 90° TO THE BEAM DIRECTION
— — — INCLUDES NUCLEAR ABSORPTION
*CARBON DATA FROM PETERSON, GILBERT AND WHITE PHYS. REV. 81 1003 (1951)
HYDROGEN
HELIUM
CARBON
d²σ/dEdΩ (90°; Eπ+) CM²(MEV)⁻¹(STERADIAN)⁻¹(EQUIVALENT QUANTUM)⁻¹(PROTON)⁻¹
Eπ+(MEV)
MU 1927

Fig. 28

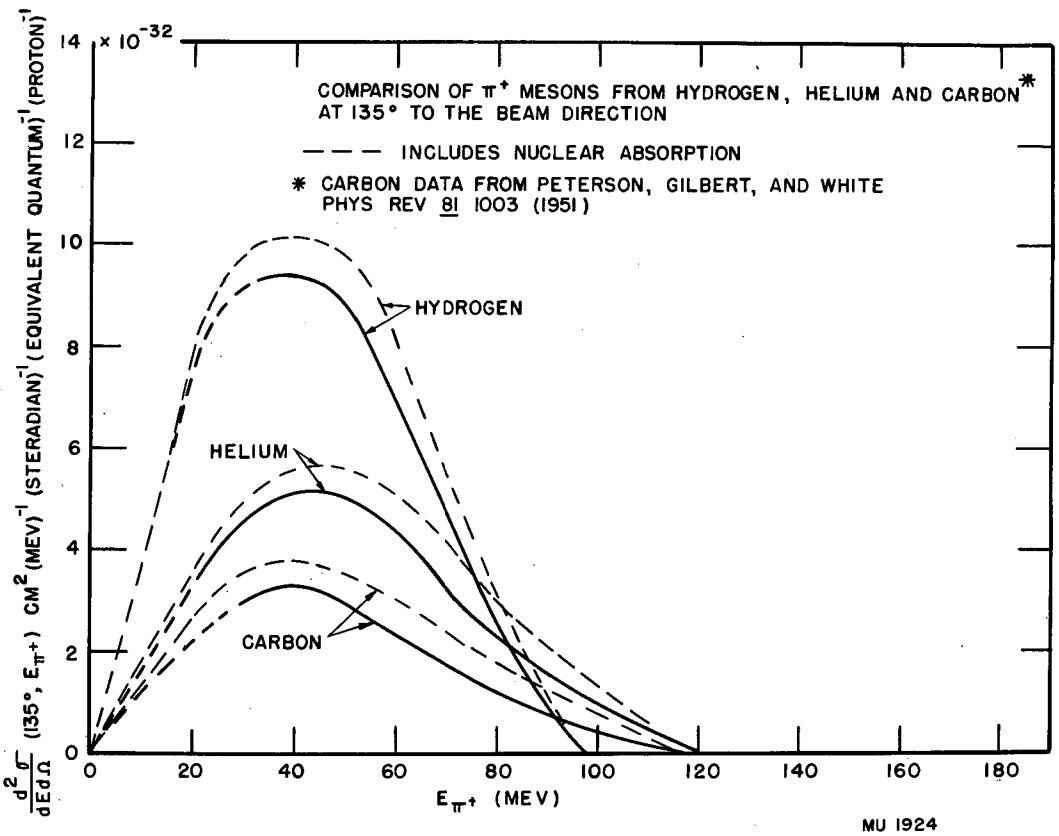
COMPARISON OF π⁺ MESONS FROM HYDROGEN, HELIUM AND CARBON*
AT 135° TO THE BEAM DIRECTION
— — — INCLUDES NUCLEAR ABSORPTION
* CARBON DATA FROM PETERSON, GILBERT, AND WHITE
PHYS REV 81 1003 (1951)
HYDROGEN
HELIUM
CARBON
× 10⁻³²
$\frac{d^2\sigma}{dEd\Omega}$ (135°, E_{π^+}) CM² (MEV)⁻¹ (STERADIAN)⁻¹ (EQUIVALENT QUANTUM)⁻¹ (PROTON)⁻¹
E_{π^+} (MEV)
0
2
4
6
8
10
12
14
0
20
40
60
80
100
120
140
160
180
MU 1924

Fig. 29